The molecular mechanism of selective and active transport in a Na^+/Ca^{2+} exchanger

Fabrizio Marinelli[1]* and José D. Faraldo-Gómez [1]*

[1]Theoretical Molecular Biophysics Laboratory
National Heart, Lung and Blood Institute
National Institutes of Health, Bethesda, MD 20814

*Correspondence should be addressed to:
Fabrizio Marinelli (fabrizio.marinelli@nih.gov) or
José D. Faraldo-Gómez (jose.faraldo@nih.gov)

Abstract

Secondary active transporters harness the electrochemical gradient of one of the substrates, typically H^+ or Na^+, to translocate molecules or ions across the cell membrane. They use an alternating-access mechanism to couple these downhill and uphill transport effectively. However, despite years of investigation, some fundamental aspects of this process still need to be elucidated. Namely, it remains to be determined the structure and energetics of relevant intermediate protein conformations along the transport cycle and how substrate binding alters them to ensure selective and active transport.

In this work, we resolve these questions for a prokaryotic homolog of the well-known cardiac Na^+/Ca^{2+} exchanger, using enhanced-sampling all-atom simulations and an original method to translate trajectory data into free-energy landscapes. We base these simulations on the available X-ray structure of the protein, which so far could be resolved only in the outward-facing state. After assessing the good convergence of the simulation data and their consistency with previous crystallographic data, we corroborate the results against available solvent-accessibility and hydrogen-deuterium exchange (HDX) measurements; the latter are examined also using a novel methodology.

The results reveal the structural features of the inward-facing conformation of the transporter and provide direct evidence for a new type of mechanism. During the alternating-access transition, ions remain bound in the center of the protein. At the same time, two pseudo-symmetric helices slide across the lipid bilayer, opening a pathway to the binding sites from one side of the membrane while occluding access from the other. Additional simulations demonstrate that the alternating access transition requires the binding of either three Na^+ or one Ca^+ ion, as only in these occupancy states the occluded intermediate conformations are energetically accessible. Overall, our results explain at the molecular level the emergence of selective and active transport in this class of transporters, in agreement with the well-established $3Na^+$:$1Ca^+$ stoichiometry.

Significance

Membrane transporters regulate critical cellular processes, ranging from substrate recruitment into the cell to ions homeostasis and signaling. Therefore, besides the general interest in rationalizing the function of these proteins, understanding their molecular mechanisms in detail is essential to identify possible inhibitors or stimulators that can be used as therapeutic agents for pathophysiological conditions. Here we used quantitative molecular simulation methods to elucidate the molecular steps of the transport cycle of a Na^+/Ca^{2+} exchanger (NCX). This protein pertains to a prominent family of membrane transporters involved in cardiac diseases. The simulation results, validated with previous biophysical and biochemical experiments, provide new fundamental insight into the transport process of the NCX family, explaining at the molecular level their known selectivity and exchange stoichiometry. Hence, the emergent mechanism presented here expands our understanding of the basic principles governing the function of secondary active transporters.

Introduction

The transport of ions and molecules across the cellular or organelle membranes is essential for cellular functions. For example, Ca^{2+} fluxes in and out of heart cells control cardiac contraction and relaxation[1, 2]. These molecular movements are often mediated by membrane pumps and transporters acting as catalysts and energy transducers, that trigger the unidirectional translocation of ions and molecules against their electrochemical gradient[3]. In secondary active transport, the membrane electrochemical (potential) gradient of a transported ion, Na^+ or H^+, provides the energy source for uphill transport. Years of investigation in this field established a consensus model referred to as alternating access mechanism[4], wherein the protein undergoes a structural change from an extracellular (or outward) to an intracellular (or inward) facing conformation intermittently exposing the bound substrates to only one side of the membrane at a time. In this manner, transport can occur under controlled conditions without futile dissipation of the ion driving force that would happen, for example, if substrates were exposed to both sides of the membrane simultaneously. Recent studies have highlighted that in most known secondary transporters, at least two stable alternating access conformations are directly encoded into the protein sequence in the form of inverted topological repeats[5-7]. X-ray or cryo-electron microscopy[3, 8, 9] have confirmed this structural dualism, albeit intermediate conformations between outward and inward-facing conformations (closed on both sides of the membrane) have been occasionally captured, for example, for EmrD[10], BetP[11] and CNT_{NW}[12].
However, other than corroborating the alternating access model, the few structural snapshots available have yet to explain their detailed mechanism of action. It needs to be understood how they achieve a selective and active transport solely recognizing specific substrates with defined stoichiometries [3]. For an antiporter, for example, the alternating access transition cannot occur in the absence of substrates bound[3, 13]. Otherwise, a leak cycle would happen, which would dissipate the ionic gradient. The premise is that binding to the correct substrate should reduce the energetic barrier for the translocation process, thereby catalyzing transport. Hence, the

nature of the intermediates of this process and how substrate binding modulates their energetics can explain this mechanism of substrate control.

Molecular dynamics (MD) simulations are one of the best suited tools to elucidate these questions. Nonetheless, long time scales (milliseconds to seconds) and large conformational changes involved in these processes have posed a particular challenge to quantitative computational studies[14]. Moreover, even for a small transporter, conventional MD detected very few unidirectional alternating access events[15], from which it is impossible to derive kinetic and thermodynamic information and exclude alternative intermediates and pathways. For common-size transporters, notable attempts resorted to hybrid strategies involving combinations of out-of-equilibrium and equilibrium simulations, in which the formers can potentially generate unrealistic high-energy atomic configurations[16-18]. Only recently, a study succeeded in describing the outward-to-inward transition of the apo state of a fast-interconverting symporter (transition time of ~1μs)[19] using short-scattered equilibrium MD simulations and Markov models. Unfortunately, such an approach might be ineffective for slower rate-limiting steps of the conformational cycle, which likely involve crossing significant energetic barriers.

In this work, we used quantitative molecular simulations methods to resolve these basic questions for a prokaryotic homolog (NCX_Mj) of the cardiac Na^+/Ca^{2+} exchanger; a membrane antiporter having a crucial role in Ca^{2+} homeostasis and signaling[20-24] and whose dysfunctions have been associated to heart diseases[25]. These antiporters function by extruding cytosolic Ca^{2+} in exchange for extracellular Na^+[26, 27] with a $3Na^+$:$1Ca^{2+}$ stoichiometry. Na^+ and Ca^{2+} electrochemical gradients are the sole determinants of transport directionality[26, 28-34]. The recently resolved outward-facing X-ray structures of NCX_Mj [13, 35] are the only available high-resolution atomic models for these types of transporters, which, based on our previous theoretical studies[13, 36], also provide the molecular basis for extracellular ions recognition. Instead, the only structural data of the inward-facing state are hypothetical low-resolution models based on the two inverted topological repeats of the protein[35, 37] or the X-ray structures of the distant Ca^{2+}/H^+ exchangers homologs[38-40]. Hence, the molecular basis of alternating access and intracellular ion recognition processes have yet to be elucidated.

To address these questions, based on the outward-facing X-ray structure of NCX_Mj, we performed extensive enhanced sampling simulations (~50 μs) in close-to-equilibrium conditions, specifically designed to explore multiple possible routes by which the alternating access transition can take place. Applying a recently proposed method for simulation analysis[41], we computed a multidimensional free energy landscape, allowing us to define the outward-to-inward pathway. The results provide direct evidence for a new alternating access mechanism that cannot be categorized within the standard rocker-switch, rocking-bundle, and elevator types[3]. Furthermore, they also provide the structural features of the unknown inward-facing state of the transporter, based on which we investigated the mechanism of intracellular ions recognition through additional enhanced sampling simulations (~70 μs). We validated the simulation results by comparison with previous measurements of hydrogen-deuterium exchange combined with mass spectrometry (HDX-MS)[42]. For that purpose, we used a new method to select the structural ensemble that best agrees with the experimental data. Additional validation was also carried out based on previous accessibility experiments[37, 42].

Overall, this work reveals the molecular details of the alternating access conformational transition of Na^+/Ca^{2+} exchangers and how the ion occupancy state of the transporter modulates the feasibility of this transition. These findings ultimately explain the emergence of selective and active transport in Na^+/Ca^{2+} exchangers.

Results

The calculated free-energy landscape reveals the alternating-access mechanism of NCX_Mj

Based on the outward facing X-ray structure of NCX_Mj (Fig. 1A) [35], we sought to determine structure and energetics of the distinct conformational states involved in the alternating access cycle, which presumably comprise the yet uncharacterized inward facing conformation. To do so, we used extensive (50 μs) atomistic simulations (Fig. 1B) coupled to a new methodology to obtain quantitative information on the conformational equilibrium, in the form of free-energy landscapes[41].

In our previous study[13], we established that apo or partial ions occupancy of the binding site locks the transporter into an outward open conformation, in which the binding site is partially accessible to bulk water. Thus, we set all the simulations according to the X-ray structure resolved at high (100-200 mM) Na^+ concentration[13, 35], in which the binding sites are fully occupied by three Na^+ ions[13, 36, 43] (Fig. 1C) and the protein adopts the transport-ready, outward-occluded conformation[13] (those simulations were also re-analyzed here; see Fig. 7AB). The MD calculations that we performed rely on a set of reaction coordinates to reversibly simulate the outward-to-inward conformational change. Here, the reaction coordinates are generally based on the pseudo-symmetry between inverted structural repeats observed in many secondary transporters[7], including NCX_Mj (Fig. 1A and Fig. S1). Specifically, they describe the linear progression of different protein regions from the X-ray structure to a repeat-swap model of the inward facing conformation[5, 8] (see methods and Fig. S1). It is worth to note that this model is only used here to define the reactions coordinates (18 in total, Fig. S2) and therefore trigger conformational changes, but is neither used as starting structure in these simulations nor is required to be a high-resolution representation the inward facing state of the protein.

The relevant conformations of the protein are revealed post-hoc by the free energy landscape in Fig. 1D, which is calculated from a novel analysis based on mean forces calculation[41]. In this map, the free energy is reported as a function of two of the previously mentioned reaction coordinates, which are related to opening/closing motions of protein regions facing either extra- or intracellular sides of the membrane (see methods and Fig. S2).

This energetic analysis demonstrates the presence of two most probable structural states of the protein corresponding to outward (OF) and inward facing (IF) conformations (Fig. 1D, Fig. 2), interconnected through a metastable region. The free energy map in Fig. 1D also shows that conformations that are fully open to both sides of the membrane are energetically forbidden, thus ruling out the occurrence of ions leakage due to water pores formation. Owing to the restraints imposed by the protein structure, conformations that are completely closed to both sides of the membrane are also unattainable (Fig. 1D).

The local stability and overall features of OF and IF states are confirmed by multi-microseconds MD simulations started from either of these states and performed without any bias potential to enhance the sampling (Fig. S3A). Namely, the average root mean square deviation (RMSD) of MD simulations started from either OF or IF states remains around 1 Å of the respective state throughout all simulations (Fig. S3B). No transitions between those two free energy minima were observed during these MD trajectories as well as during the enhanced sampling simulations (~6 μs) that we later performed to investigate the mechanism of intracellular ions recognition (Fig. 7), which confirms the presence of a significant free energy barrier for the OF-to-IF transition.

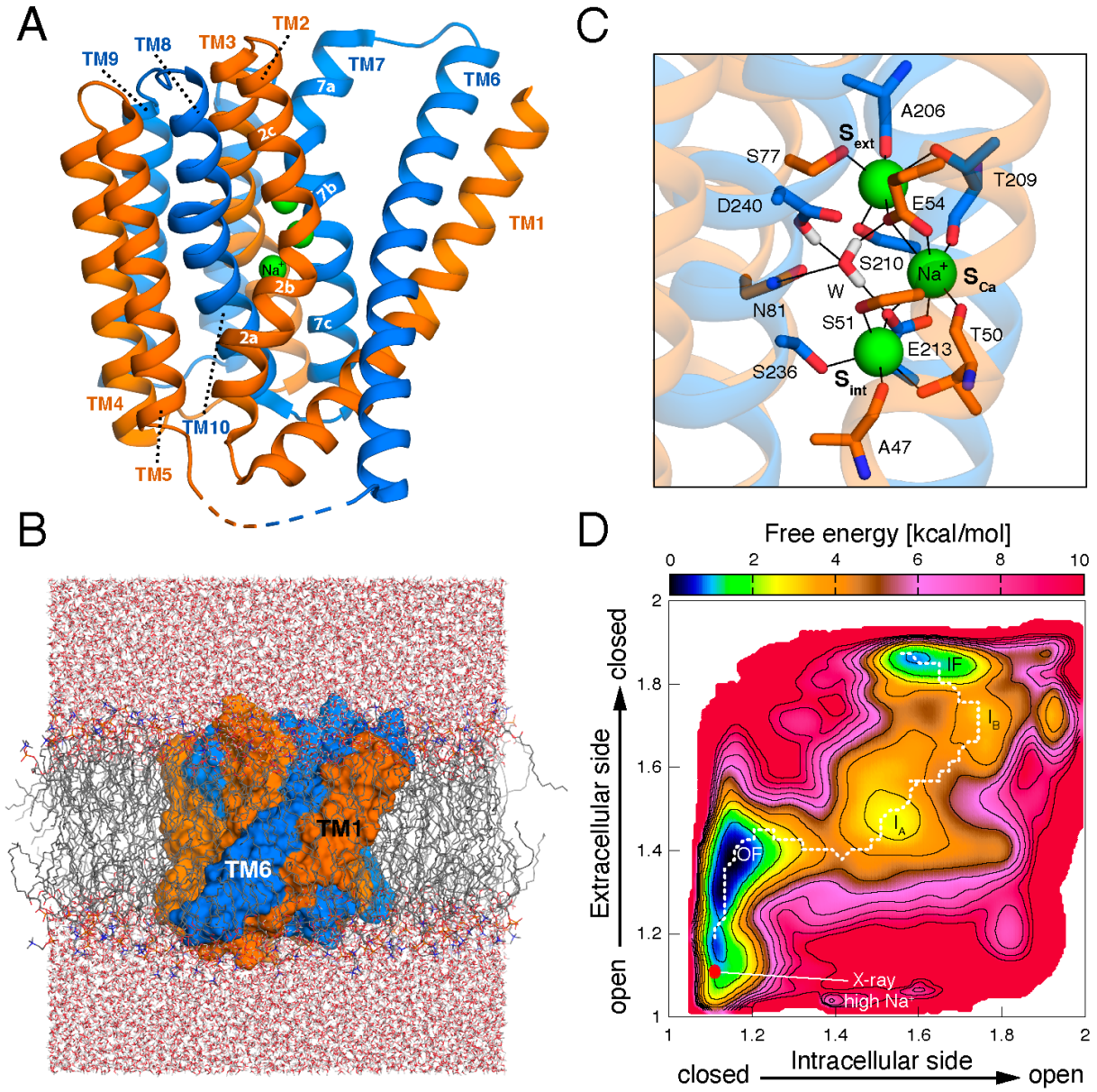

Figure 1. Structures and free energy landscape of the Na^+/Ca^{2+} exchanger from M. jannaschii. (A) Cartoon representation of the outward-facing X-ray structure of NCX_Mj[35].The folding topology consist of two inverted-repeats displayed in orange and marine respectively. The protein is bound to three Na^+ ions[13, 36] indicated by green spheres. (B) All-atom simulation system enclosed in a rectangular prism periodic box, comprising NCX_Mj bound to three Na^+ ions, with D240 protonated (as shown in panel C). The protein was embedded in a POPC lipid bilayer (208 molecules) and solvated with 14892 water molecules and Cl^-

counterions (omitted for clarity). (C) Close-up of the binding site. Protein residues and the water molecule surrounding the Na^+ ions are highlighted in sticks representation. (D) Conformational free energy landscape of the alternating access transition of NCX_Mj, calculated using bias exchange metadynamics[44] a mean-force approach[41] (see methods). The map represents the free energy as a function of two path collective variables (ξ_6 and ξ_{13} in Fig. S2). Contours are shown in intervals of 1 kcal/mol. Red circles map the X-ray structures obtained at high Na^+ concentration[13, 35] (pdb entries 3V5U, 5HXE). The main free energy minima (OF and IF) and intermediate metastable regions (I_A and I_B) are indicated. The two-dimensional projection of the minimum free energy path (dashed white line) connecting OF and IF states (see Fig. 6) is also shown. The error estimate of the calculated free energy map is provided in Fig. S4A.

The outward-facing state entails a broad set of conformations comprising the X-ray structures

Previous crystallographic data captures the exchanger in an outward facing (OF) conformation[13, 35], which, according to the alternating-access transport model [4], ought to represent one of the main structural arrangements of the transporter. Our results support this notion, revealing that the outward facing (OF) state corresponds to the most probable region of the free energy landscape (~86% probability, Fig. 1D and table S2).

The OF state entails an ensemble of outward exposed conformations (Fig. 2A and Fig. S5), resembling the Na^+ bound X-ray structures[13, 35, 36], with an average C_α RMSD from the latter of 1.76 Å (excluding loop regions). This notwithstanding, the OF region features wide-ranged opening/closing fluctuations of the extracellular protein region and to a lesser extent of the intracellular one, that are associated to conformational motions of TMs 1,6 and 7 (Fig. S2). In particular, TM7 can adopt either α-helical (~70% probability) or unstructured/kinked (~30% probability) conformations. Such variability results in pairwise structural differences among OF configurations ranging from 0.5 Å to 2.5 Å of RMSD (grey line in Fig. 3A). The X-ray structures of NCX_Mj bound to three Na^+ ions[13, 35, 36] correspond to energetically feasible configurations of the OF state (Fig. 1D and Fig. 2CE) that, compared to the average OF conformation, entail a slightly wider extracellular opening in which TM7 is captured in a kinked arrangement (Fig. S5, Fig. S8D).

In agreement with our previous work[13], extracellular exposure stems from two aqueous channels (Na^+ and Ca^+ channels, Fig. 2A) that penetrate near the binding site region, whereas waters are mostly excluded from the intracellular one. It is worth noting that, owing to the full occupancy of the binding sites by 3 Na^+ ions, these sites remain shielded from the solvent[13] (see also Fig. 7AB).

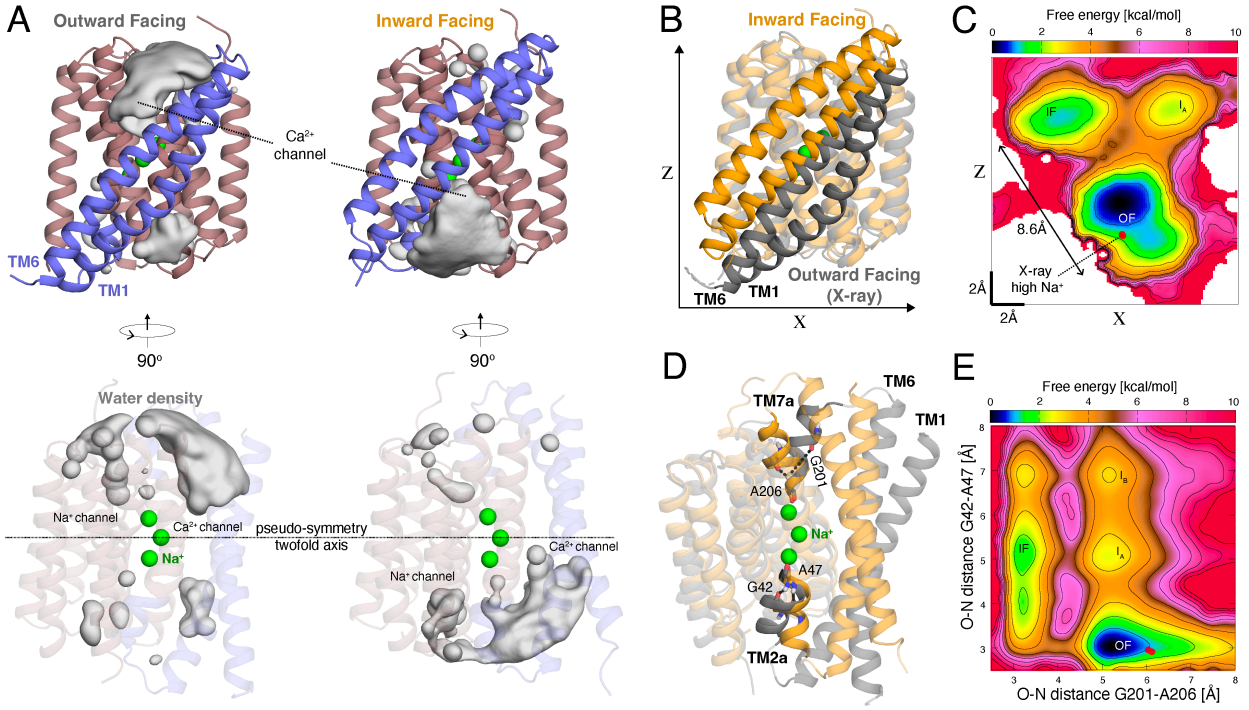

Figure 2. Structural features of the main energetic minima of the conformational free energy landscape of NCX_Mj. (A) Representative protein conformations of OF and IF free energy minima of the free energy landscape (Fig. 1D), illustrated in cartoon representation (the spheres denote the Na^+ ions). The isosurface of the density of waters that are within 12 Å of the protein binding sites is shown as grey volumes. The protein scaffold (TM2bc, TM3-5, TM7bc, TM8-10, dirtyviolet) and moving helices (TM1, 6, TM2a, 7a, slate) are shown in different colors. (B, D) Cartoon representation of an IF reference conformation (bright orange) and the X-ray structure solved at high Na^+ concentration (pdb entry 3V5U[35], grey), superimposed on scaffold regions. X and Z axes in panels B and C approximate parallel and orthogonal directions to the membrane plane, wherein X reflects the direction of the axis connecting the centers of TMs 4 and 9, whereas Z represents the average vertical axis of these two TMs (see methods). (C) Free energy surface of TMs 1,6 center projected along X and Z directions (see methods), using the same representation of Fig. 1D. (E) Free energy as a function of O-N backbone distances for G201-A206 and A43-A47 pairs. The associated O-H distances are indicated as black dotted lines in panel D. Intermediate conformations (I_A and I_B) between OF and IF states (see Fig. 6) are indicated on the maps of panels C and E. Error estimates on the latter maps are provided in Fig. S4BC.

Energetic analysis identifies a well-defined inward facing state resembling CAX_Af structure

The notable consistency between OF conformations arising from simulation and crystallographic data, supports the application of our computational analysis for the structural assessment of other relevant conformations of the transporter. In this regard, the free energy landscape reveals that the transporter can adopt a second, significantly populated structural state (~12% probability, Fig. 1D and table S2), clearly distinct from OF conformations (clear-cut separation between pairwise RMSD distributions of OF-to-IF and either of OF-to-OF and IF-to-IF in Fig. 3A). Further analysis of this free energy minimum demonstrates that it corresponds to a well-defined IF state of the transporter (Fig. 2), thus confirming the expectation that NCX mediates Na^+/Ca^+ exchange through an alternating-access mechanism. Importantly, structures pertaining to the IF region of the map (Fig. 1D) resemble qualitatively the IF repeat-swap model (Fig. 3C, $\langle RMSD \rangle$=2.6 Å, repeats identity 31.4%) and the inward facing X-ray structure of the related Ca^{2+}/H^+ exchanger [40], from *A. fulgidus* (CAX_Af, Fig. 3D, $\langle RMSD \rangle$=3.2 Å, sequence identity 20.4%; see also table S2).

In contrast to the OF state, protein conformations pertaining to this energetic minimum feature a markedly compact arrangement of the outward facing region, which largely precludes extracellular water entrance. Conversely, the protein is structurally open and water accessible on the cytosolic side (Fig. 2A), through two aqueous channels (Na^+ and Ca^{2+} channels) which appear somewhat symmetrical to those present in OF conformations (Fig. 2A), according to a twofold axis parallel to the membrane plane (as per the inverted-repeats fold[5, 8]). As in the OF state, the binding site region remains poorly solvent accessible, hence the IF free energy minimum reflects an inward occluded state of the protein. Overall, the IF ensemble is structurally more compact than the OF one, comprising fewer overall fluctuations (pairwise RMSD<2 Å; bright orange line in Fig. 3A), mostly related to transitions between π- and α-helical arrangements of TM2A and compact extended conformations of the loop between TM1 and TM2. To assess more accurately the energetics of those arrangements, we performed additional free energy calculations, showing the that they are approximately isoenergetic (see Fig. S6 and supporting text).

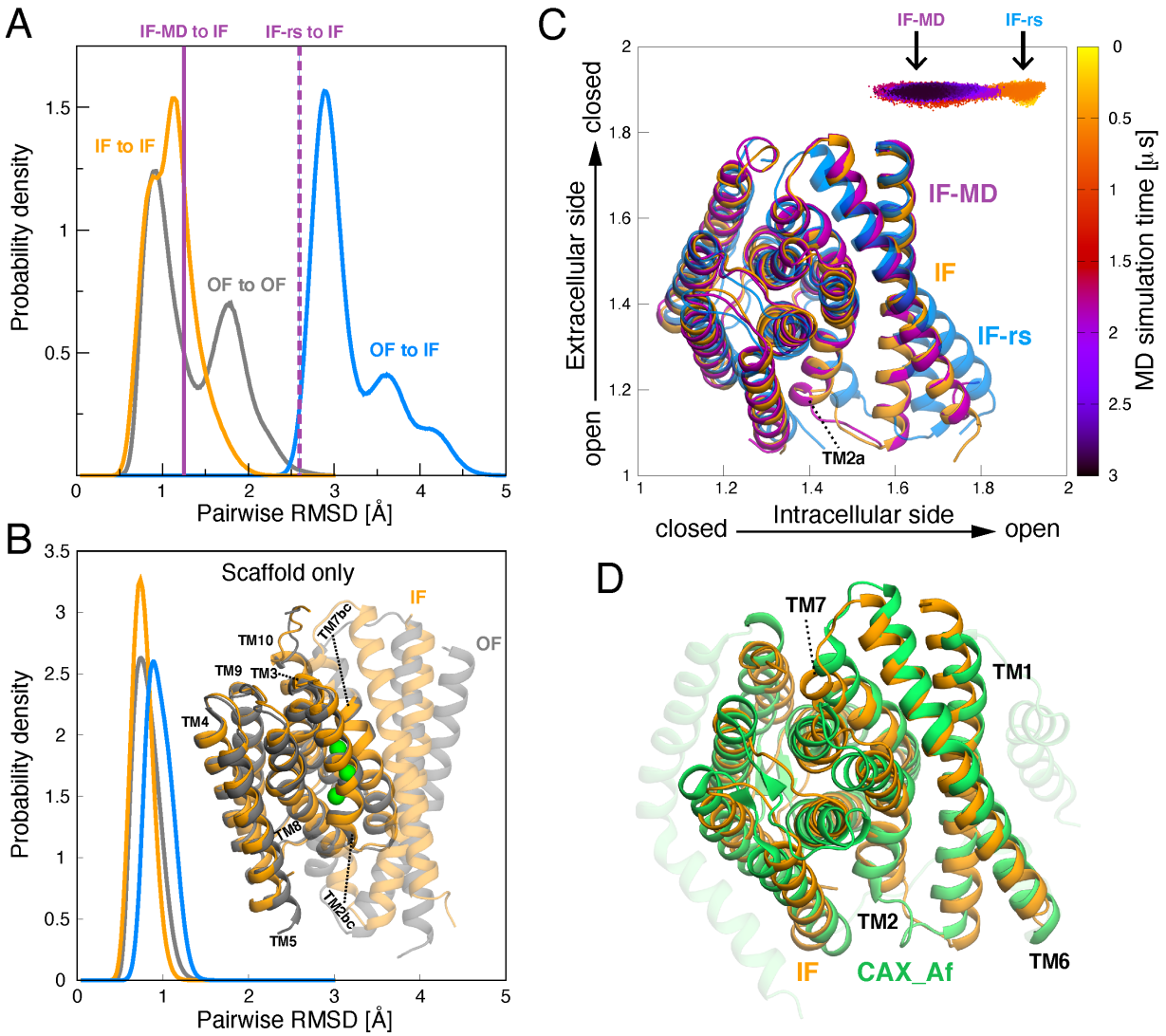

Figure 3. Structural features, comparisons and consistency of the main energetic minima of NCX_Mj. (A) Pairwise RMSD distributions (only Cα atoms, with loop regions excluded) of conformations pertaining to OF (orange line) and IF structural ensembles (grey line) or between OF and IF states (blue line). The average RMSD between IF and MD (> 1.5 μs) or RS model conformations is shown as solid and dashed purple lines respectively. (B) Analogous pairwise RMSD distributions (as in panel A) including scaffold regions only (excluding TM1, TM2a, TM6 and TM7a). The overlay between the IF reference structure and the NCX_Mj X-ray structure at high Na^+[13] (pdb entry 5HXE), aligned on scaffold regions, are illustrated in cartoon representation. (C) MD simulation sampling mapped on the same reaction coordinates of Fig. 1D. IF and MD conformations featuring lowest mutual RMSD (< 1 Å) and their overlay with the repeat-swap model (IF-rs) are shown. (D) Superimposition between CAX_Af X-ray structure (pdb entry 4KPP[40]) and reference structure of the IF state using cealign [45, 46].

MD simulations based on a repeat-swap model confirm the proposed inward-facing state

Building upon the similarities between repeat-swap model and conformations pertaining to the IF free energy minimum (Fig. 1D), we set out to devise an independent control of structure and local stability of the latter. Specifically, we employed a conventional MD calculation initiated from the repeat-swap model, according to a distinct simulation setup (see methods).

By construction, protein arrangements closely resembling the repeat-swap model feature values of the reaction coordinates that approach their upper boundary value, 2 (see methods), which however lies on a metastable region of the free energy map (Fig. 1D). Consistently, after 0.5 μs, the MD simulation drifts from the repeat-swap model (Fig. 3C and Fig. S7) and converges towards conformations that map onto the energetically feasible region of the IF state (Fig. 1D and Fig. 3C) and that are in remarkable agreement ($\langle \mathrm{RMDS} \rangle$ < 1.3 Å and pairwise RMSD ranging from 0.8 to 2 Å) with structures therein (Fig. 3A and Fig. S7). However, while the enhanced sampling calculations capture both π-helical and α-helical arrangements of TM2a (Fig. S6 and Fig. S8D), only the latter is sampled in the limited time scale of the MD simulation. In summary, all our simulation data point to the IF state derived from the free energy analysis as the consensus computational model of the inward facing conformation of NCX_Mj.

Outward-to-inward transition entails sliding of TMs 1,6 and rearrangement of TMs 2a,7a

The comparison between outward and inward facing states derived from the calculated free energy landscape reveals a considerable structural variation in the transporter throughout the alternating-access transition (Fig. 2BD). In particular, the conformational switch from OF-to-IF is characterized by large-scale rearrangements of the pseudo-symmetric pairs (Fig. S1), TM1, 6 and TM2a, 7a, relative to an essentially rigid scaffold (Fig. 2BD and blue lines in Fig. 3AB). The latter scaffold also entails the binding sites region, consistently with the observation that OF and IF states are Na^+-bound occluded conformations. The most significant change is a displacement of TM 1 and 6, across the membrane (Fig. 2B), as detailed by an alternative free energy landscape specifically mapping those transmembrane movements (Fig. 2C). Besides recapitulating the main energetic minima described previously (Fig. 1D), this map underscores that during the interconversion between OF and IF states, TM 1 and 6 undergo a diagonal sliding motion spanning overall ~1 nm range (Fig. 2C). This translational movement of TM1, 6 has been previously hypothesized based on the inverted pseudo-symmetry of NCX_Mj topological repeats[7, 35, 47, 48] and from the inward facing X-ray structures of Ca^{2+}/H^+ exchangers[38-40], which pertain to the same transporter's family[49] (CaCA superfamily). Our work provides the first detailed atomistic description of this type of conformational mechanism, showing how it regulates opening and closing of intracellular and extracellular Ca^{2+} channels (Fig. 2AB and Fig. S8ABC) and how it is coupled with TM2a and TM7a rearrangements that instead control the water accessibility through Na^+ channels (Fig. 2AD and Fig. S8). The conformational changes of TM2a and TM7a can be monitored by the disruption/formation of the pseudo symmetric (Fig. S1) H-bonds between residues G42-A47 and G201-A206 (Fig. 2D). Specifically, the free energy surface as a function of these H-bond distances (Fig. 2E) reveals that, during the OF-to-IF transition, TM7a undergoes a structural change from a flexible arrangement, encompassing α-helical, unstructured, and kinked conformations, to a well-defined, partially π-helix conformation, characterized by the formation of the G201- A206 H-bond (Fig. 2D and Fig. S8D). Upon these rearrangements, TM7a loses on average 2.5 α-helical residues (out of 6.3 in the OF state) and 4.8 residues adopt a π-helix conformation (out of 0.4 in the OF state). Concurrently, a portion of TM2a transitions from the analogous, topologically inverted, π-helix conformation to a less

structured arrangement, comprising α- or π-helix (Fig. S6), in which the G42-A47 H-bond becomes disengaged (Fig. 2D and Fig. S8D). The partially π-helical conformation of TM2a in the IF state entails on average 4 residues in π-helix conformation while 3.9 residues are α-helical.
The structural changes of TM2a, 7a during the OF-to-IF transition led to the closure of the extracellular Na^+ channel and opening of the intracellular one (Fig. 2 and Fig. S8AB). Overall, the observed rearrangements of TM1, 6 and TM2a, 7a, are reversible, interconnected and altogether mediate the alternating access transition of NCX_Mj.

Previous accessibility and HDX-MS data supports the outward-to-inward structural change derived from the simulations

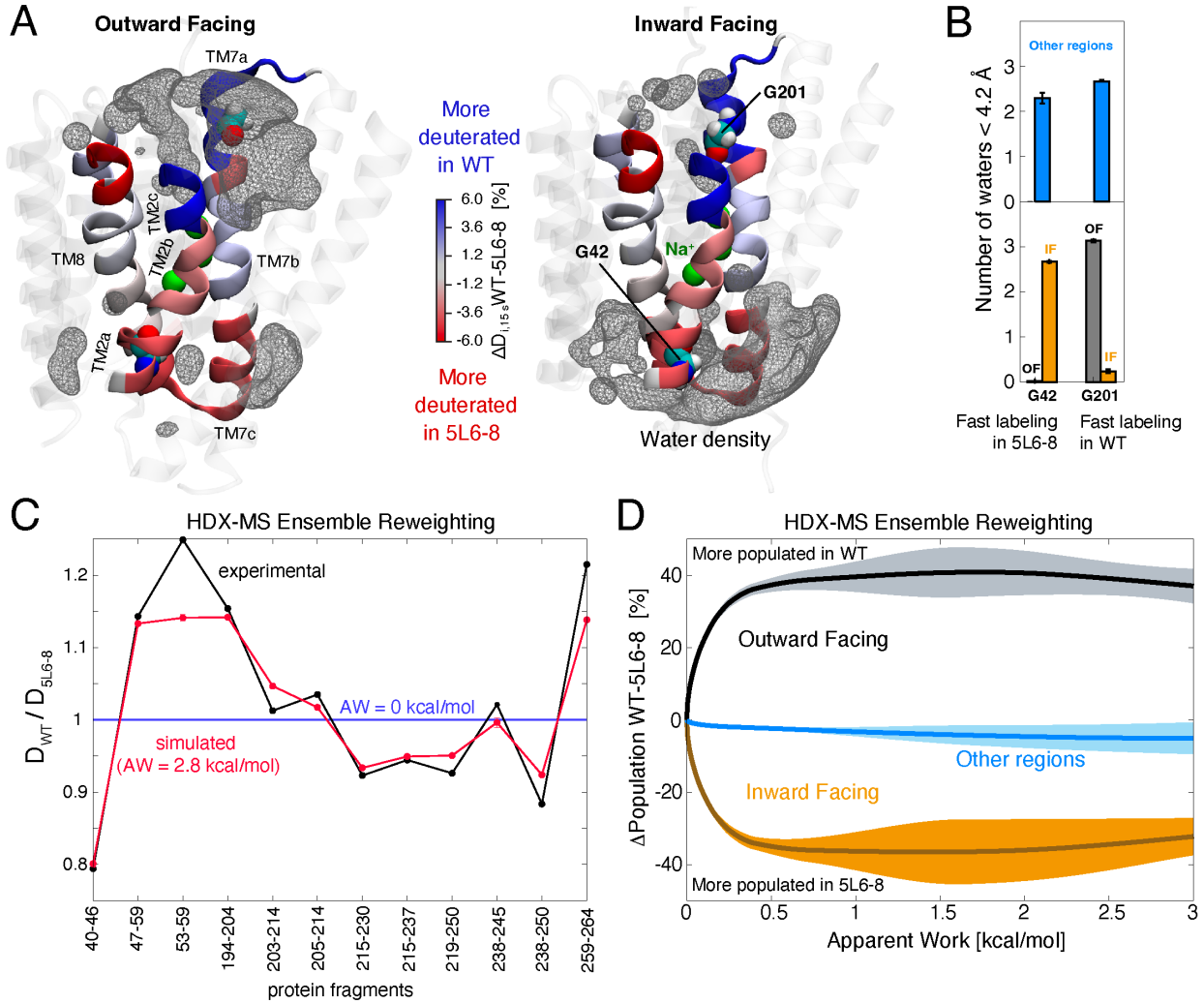

Figure 4. Validation of the simulation results based on accessibility and HDX-MS data. (A) Cartoon illustration and density isosurface of waters within 12 Å of the protein binding sites (gray mesh) for OF and IF states. Green spheres denote Na^+ ions. Residues G42 and G201, referred to cysteine accessibility measurements on NCX_Mj[42] are represented as spheres. Protein regions for which HDX-MS data on NCX_Mj[42] are available (TMs 7, 2 and 8) are highlighted. The color gradient (from blue to red) reflects the difference between WT and 5L6-8 deuterium uptake levels, for different protein fragments[42], upon 15s deuteration time. For illustration purposes, data on overlapping protein fragments has been broken down into smaller non-overlapping regions by linear combination of the deuterium fractions. (B) Average number of waters within 4.2 Å of residues G42

and G201 for OF, IF and other regions of the free energy landscape (Fig. 1D). Error bars reflects the statistical uncertainty estimated through block analysis. (C) Ratio between WT and 5L6-8 deuterated fractions measured at 15s (deuteration time) for the experimentally detected protein fragments (denoted by the residue ranges). The black dots denote the experimental data[42], whereas the red dots are the predicted ratios at an average apparent work of 2.8 kcal/mol (see supporting text). As the starting conformational ensemble is the same for either WT or 5L6-8 target data, the initial predicted ratio is one when the apparent work is zero (blue line). (D) Trend of OF, IF and transition regions relative populations (see Fig. 1D) as a function of the total apparent work, upon ensemble reweighting with HDX-MS data (see supporting text). The plot reports the difference between the populations obtained by targeting either WT or 5L6-8 HDX-MS measurements, in which the shaded area reflects the statistical error obtained by blocks analysis.

In absence of high-resolution crystallographic or cryo-electron microscopy data on the IF state of NCX, we set out to assess the reliability of the simulation results using existing physiological and biophysical data. To this end, we focused on previous accessibility and HDX-MS measurements[42], which can be directly compared with the simulation data. The experiments that we considered are based on wild type (WT) NCX_Mj and a specific functional mutant, 5L6-8, characterized by eight residues elongation of the short intracellular loop connecting TM5 and TM6 (dotted loop in Fig. 1A)[47]. Measurements of apparent Ca^{2+} and Na^{+} affinities (K_m) to outward and inward facing sides of the protein suggest that wild type (WT) NCX_Mj preferentially adopts an OF conformation[43, 47] (in agreement with the crystallographic data[13, 35]), whereas a cytosolic facing arrangement seems predominant in the 5L6-8 mutant [47]. Hence, the latter mutant could be used for the structural characterization of the IF state of NCX_Mj.

The available cysteine accessibility measurements for NCX_Mj refer to residues G42 and G201[42] (Fig. 4A), that are located on TM2a and TM7a respectively, in pseudo-symmetric positions of the two topological repeats (Fig. S1). Covalent labeling of cysteine mutants with a fluorescent probe (TMRM maleimide), in detergent preparations, showed that residue G201 is more accessible than G42 in the WT protein, while the opposite is true for the 5L6-8 mutant. Consistently, our simulation data shows that residues 42 and 201 are alternatively water exposed during the OF-IF interconversion (Fig. 4AB), which is in agreement with the opposite preference of WT NCX_Mj and 5L6-8 mutant for OF and IF conformations[42]. Notably, these two residues are approximately equally water exposed in conformations pertaining to the transition region between OF and IF states (other regions in Fig, 4B). Hence, as predicted by our free energy landscape, they ought to correspond to low probability conformers (1-2% probability based on the free energy map in Fig. 1D) providing a negligible contribution to the accessibility of those residues.

The other experimental technique that we used to validate the simulation data is HDX-MS, which is a powerful complementary approach to characterize the conformational dynamics of secondary transporters[50]. Recent HDX-MS measurements on WT and 5L6-8 NCX_Mj provided substantial structural information on α-repeats regions (Fig. 4A), in the form of time course of deuterium incorporation[42, 51]. Provided global protein unfolding can be neglected (EX2 exchange), the deuteration rates can be correlated with the local degree of solvent exposure and structural flexibility. To limit the contributions of non-local, protein unfolding processes to the rate of deuterium absorption (EX1 type exchange) [42, 51] (which hinder quantitative structural analysis), here we focused on data obtained after short time exposure to D_2O (15 s). For HDX-MS measurements recorded under saturating Na^{+} concentration[42], i.e. those that mimic more closely the simulation conditions (binding sites fully occupied by Na^{+}), the data underlines larger

intracellular deuteration levels for the 5L6-8 mutant compared WT, whereas, except for the C-terminal portion of TM8, the opposite trend is observed for extracellular regions (Fig. 4A). This trend of WT vs 5L6-8 deuteration levels (Fig. 4A) are qualitatively in line with the notion that the 5L6-8 mutation switches the conformational probability favoring the IF state. Nonetheless, this data alone does not clarify whether and to which degree OF and IF structural ensembles predicted by the simulation agree with the HDX-MS data.

To this end, we applied a new variant of our recently proposed maximum-entropy approach to combine the atomistic simulations with the HDX-MS data[52]. Specifically, the methodology is based on a minimal adjustment of the population of each region of the free energy landscape, so that the resulting structural ensemble conforms to the HDX-MS data up to a given level of error (see supporting text). To do so, we relied on an established model, based on amide H-bonds and atomic packing content[53], to predict the deuteration rate of different protein regions in each configuration of the free energy landscape. To reliably compare predicted and experimental measurements, we developed a new formulation that considers explicitly the presence of an unknown percentage of deuterium loss during the experimental preparation (after quenching the exchange reaction) [54, 55]. Such new scheme is particularly relevant for cases, such as our target data (personal communication), where there has been no experimental determination of the deuterium loss (data are not back-exchange corrected) and the latter can be reasonably assumed to occur in the same proportion in WT and mutant protein[55] (see supporting text).

The results of this reweighting methodology reveal that a close agreement with the experimental data (Fig. 4C) can be obtained by a population shift associated to the 5L6-8 mutation (requiring apparent work to be applied as shown in Fig. S9), wherein the IF state probability increases significantly when fitting to the 5L6-8 data relative to that of the WT, compensated by the opposite trend in the probability of the OF state (Fig. 4D). Conversely, the probability of protein conformations pertaining to the transition region between IF and OF states is not significantly affected by this reweighting procedure (other regions in Fig. 4D). Hence, simulations and experiments provide substantial evidence that the 5L6-8 mutation reshapes the free energy

landscape favoring the IF state of the protein and that the latter state (as well as the OF state) is well-represented by the model derived from our simulations.

Outward-to-inward transition entails alternating disruption and formation of hydrophobic, electrostatics and protein/lipid contacts out of the binding site region

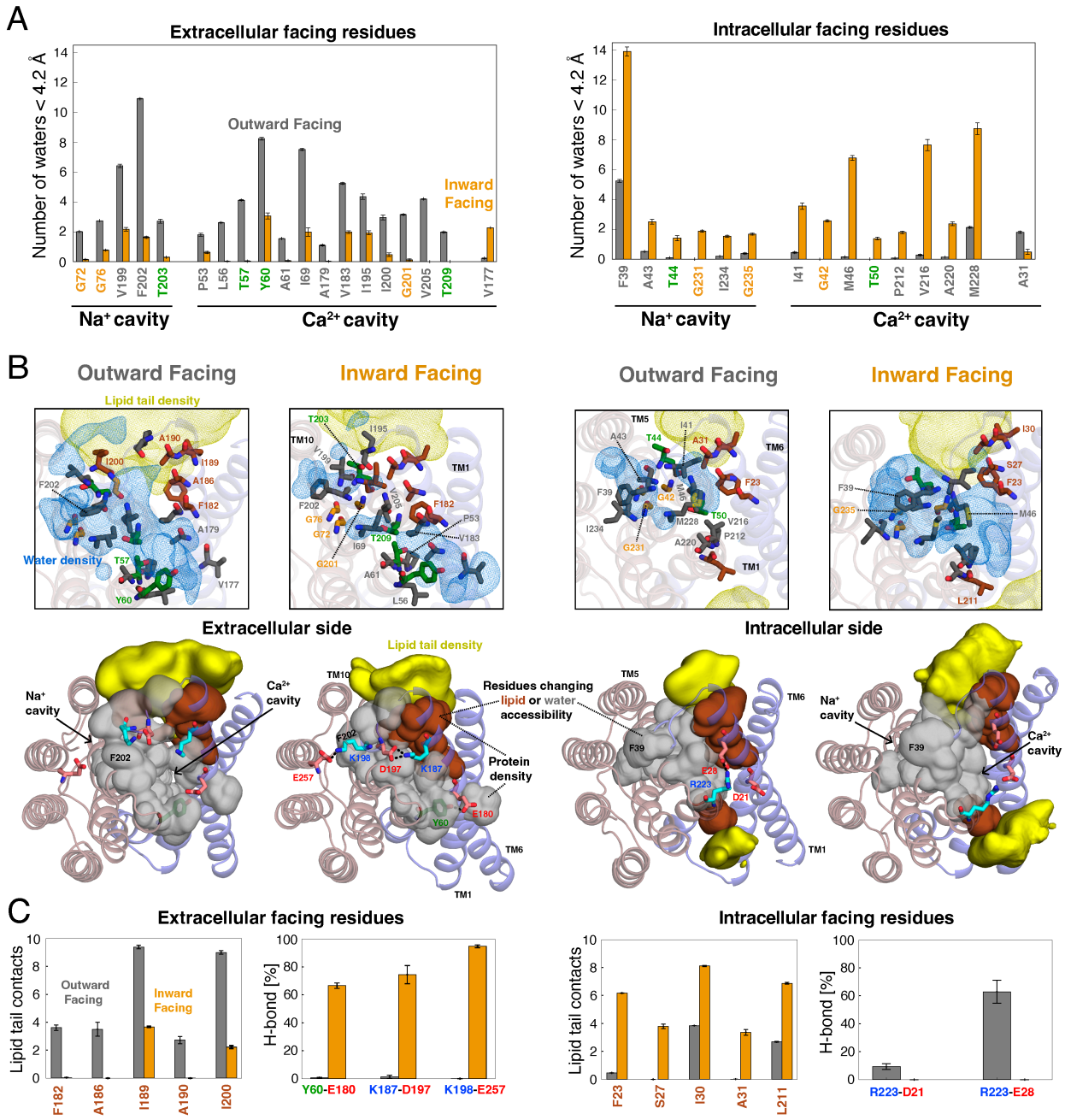

Figure 5. Per residue analysis of the main interaction patterns that form and disrupt during the outward-to-inward conformational transition. Reported quantities are calculated for outward- as well as inward-facing structural ensembles derived from the free energy analysis (Fig. 1D). (A) From left to right the panel shows the number of water molecules within 4.2 Å of either extra- or intracellular facing residues (only the apolar portion of the sidechain; see caption of Fig. S10) that undergo a significant change in water accessibility during the outward-to-inward transition (only changes by at least a factor of two are included). (B) From

left to right the panel shows representative structures indicating either extra- or intracellular facing residues that undergo a significant change in water accessibility (panel top: grey, green, and dark-yellow residues), lipid contacts within 5.2 Å (panel top: brown residues) and h-bond fraction (panel bottom: red and bright blue residues) during the OF to IF transition. The density isosurfaces of water molecules within 4.2 Å and lipid tails within 5.2 Å of the associated residues is shown as blue mesh and yellow mesh (panel top) or volume (panel bottom) respectively. At the panel bottom, the density volume of residues changing water accessibility and lipid contacts upon OF-to-IF switch are shown as grey and brown volumes respectively. (C) Number of lipid contacts and H-bond fractions (based on 3.2 Å distance cut-off between heavy atoms) of the previously mentioned extra- (panel left) and intracellular facing residues (panel right). The number of lipid contacts considers only the lipid tails within 5.2 Å of either extra- or intracellular residues featuring significant change in lipid exposure during the outward-to-inward transition (we excluded hydrogen atoms and polar groups as detailed in the caption of Fig. S10).

The coexistence of at least two distinct conformational states in a secondary active transporter, as established by the alternating-access mechanism[4], requires a strict balance between the interactions that are formed and disrupted during the OF-to-IF conformational switch, such that both states are energetically feasible. The presence of inverted topological repeats in most of the known secondary transporters[5, 7, 8] would potentially explain this balance in terms of topologically inverted interaction patterns in OF and IF states. Nevertheless, the low sequence similarity between the two repeats and/or an asymmetric environment[7] may lead to complex compensation mechanisms involving asymmetric contributions of protein/protein, water/lipid-mediated interactions and in some case even membrane deformations[56]. Given that the derived free energy landscape predicts the presence of two significantly populated OF and IF states of NCX_Mj and that these conformations are in reasonable agreement with the available crystallographic, biochemical, and biophysical data, we posit that it ought to be possible to rationalize the structural basis for this interaction fine-tuning from post-simulation analysis.

To do so, we extracted the protein residues featuring a significant change in lipid/water accessibility and in H-bonds formation between OF and IF states. To highlight the role of electrostatic and hydrophobic interactions, we separated the contribution of polar and apolar groups in amphipathic protein residues as well as in lipid molecules.

This analysis identifies a set of apolar groups, largely pertaining to hydrophobic residues, that are alternatively water exposed during the OF-to-IF conformational switch (Fig. 5A). In the OF state, the energetic cost arising from water exposure of extracellular apolar groups (except for V177) is partially compensated by water exclusion from the intracellular ones (except for A31). The opposite trend is instead observed for IF conformations, thus generating a substantial balance between the hydrophobic interactions stabilizing these two states (Fig. 5AB and Fig. S10AB). Additionally, we identified two set of residues, most of them pertaining to TM1/6 (extracellular and intracellular brown surfaces/residues in Fig. 5BC), that, during the translational movement of the latter pair of helices (Fig. 2), switch hydrophobic contacts between protein and lipids (Fig. 5BC) and in this manner lead to opening and closing of Ca^+ water channels at the opposite sides of the membrane. Notably, these two sets of residues also entails pseudo symmetric pairs such as F23 in one group and F182 in the other (Fig. 5BC, Fig. S8C and Fig. S1). Concurrently, the movements of TM7a and TM2a (Fig. 2) induce the formation and disruption of apolar contacts in Na^+ channels regions, with notable rearrangements of F202 and F39 residues that are alternatively buried in extracellular and intracellular hydrophobic pockets respectively (Fig. 5AB and Fig. S8C).

This analysis also reveals that OF and IF states are stabilized by alternative sets of salt bridges and H-bonds (Fig. 5BC, Fig. S10CDE) as well as water solvation of polar residues, none of which involves the binding site region. Specifically, the hydroxyl group of T44 become water accessible

during the OF to IF transition while the opposite effect is observed for the hydroxyl groups of T57 and T203. Further analysis on how the charges of these polar groups reshape the free energy landscape shows that indeed this energetic term favors the OF state over the IF one while the opposite trend is observed for H-bonds and salt bridges, leading overall to a compensating effect (see Fig. S10E and supporting text). Conversely, we observed neither significant changes in H-bond formation between protein and lipids nor drastic variations in the membrane deformation and thickness (which remain within 2-3 Å; see Fig. S11) during the alternating access transition. It is worth to note that most protein residues that change accessibility to water or lipid and part of those involved in alternating polar contacts are homologous across repeats (Fig. S1). The implication is that a considerable portion of the energetic balance generating two well populated alternating conformations arises from the presence of topologically inverted interaction groups. Particularly notable is also the conservation across repeats of glycine residues that change water accessibility during the OF-to-IF transition and that enable close packing of TM2-TM8 in the OF state (G72, G76, G201) and the topologically inverted pair, TM7-TM3, in the IF one (G231, G235, G42; Fig. S8A).

The transition between OF and IF occluded states occurs through closed intermediates and surmountable energetic barriers

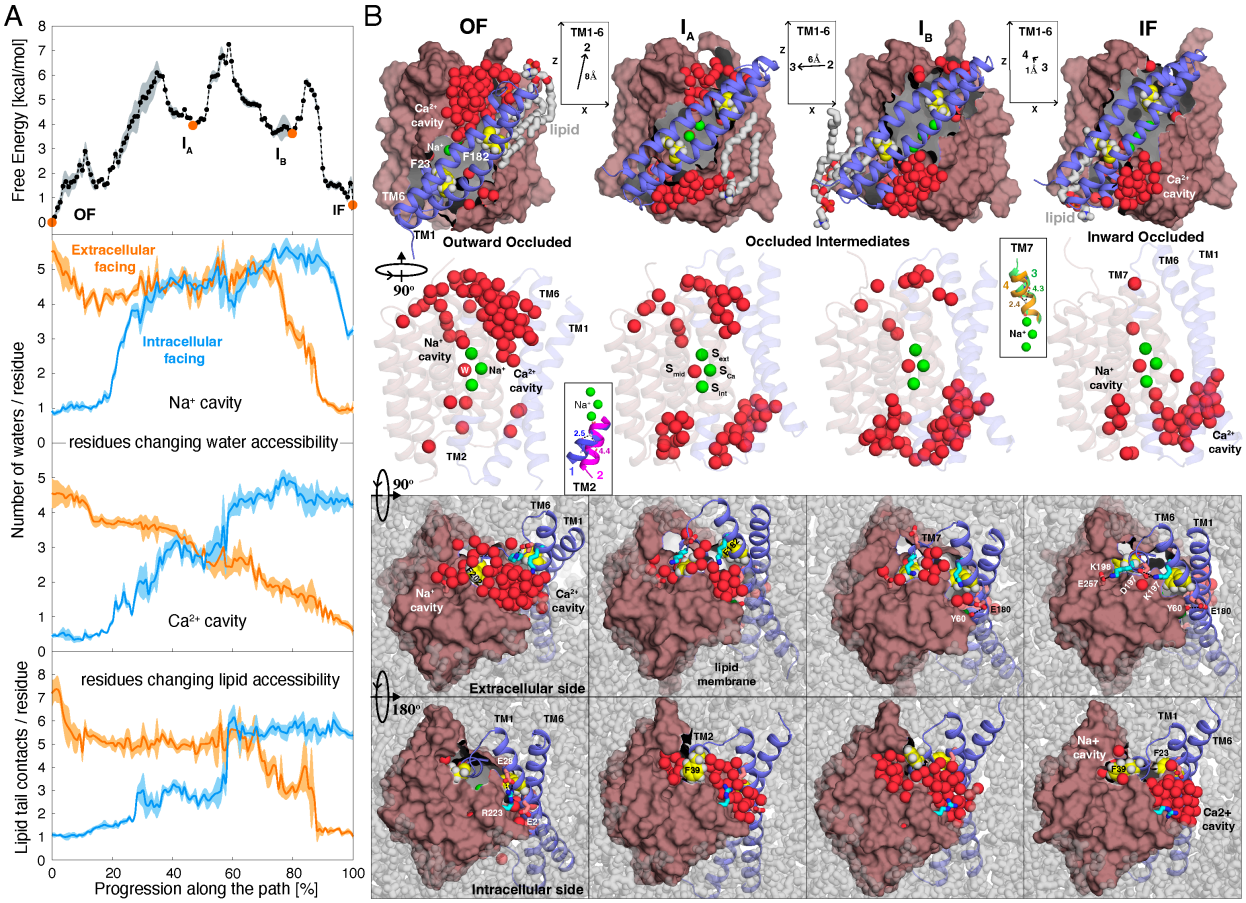

Figure 6. Microscopic mechanism of the alternating access transition in the Na^+/Ca^{2+} exchanger. (A) Calculated thermodynamic and structural properties along the most likely transition pathway between OF and IF states (see methods): from top to bottom;

free energy, number of water molecules per residue within 4.2 Å of the latter for the indicated protein cavities (see also Fig. 5) and number of lipid tail contacts per residue (within 5.2 Å, see Fig. 5 caption). The shaded areas reflect the statistical error calculated through blocks analysis. The calculated structural properties reflect configurations close to the most likely transition pathway according to a small distance cutoff (corresponding to three bin sides in collective variable space; see methods) and selected based on a Monte Carlo algorithm to conform to the 8-dimensional free energy in the direction orthogonal to the path. (B) Representative structures along the OF-to-IF transition pathway. Water molecules within 12 Å of binding site residues and Na^+ ions are shown as green and red spheres respectively. The two top panels outline lateral membrane views. At the panel top, lipid molecules near F182 and F23 residues (shown as spheres with yellow carbon atoms) are depicted as sticks with grey carbon atoms. The two bottom panels show intra- and extracellular views with F23, F39, F182 and F202 side chains shown as spheres and those involved in H-bonds/salt-bridge formation/disruption during the transition shown in sticks representation (light blue and red residues). The protein scaffold (dirtyviolet surface or cartoon) and moving helices (slate cartoon) are shown in different colors. The insets highlight movements of TM1-6 in the x,z plane (as reported in Fig. 2) and structural changes of TM2a and TM7a with G42-A47, G201-A296 backbone H-bonds indicated as dashed lines.

Further analysis of the enhanced sampling simulations permits to elucidate how the alternating access transition occur. To do so, we considered comprehensive set of reactions coordinates (eight in total), describing the conformational changes of TMs 1, 6, 2a, 7a and connecting loops as well as side chain rearrangements of Na^+ and Ca^{2+} channels regions (see methods). Based on this set of variables we derived the most probable free energy pathway between outward and inward facing states, describing in detail all the relevant intermediate steps of the alternating access transition.

Free energy, structural patterns, and a set of representative conformations along this pathway are shown in Fig. 6. Starting from the outward occluded state (OF state in Fig. 6), the first stage of the transition entails partial opening of intracellular Na^+ and Ca^{2+} cavities permitting water entrance into the latter, whereas extracellular cavities are less affected by these changes. These structural rearrangements are assisted by opening movements of TM1-TM6 and TM2a, wherein the latter TM region, after dissociation of F39 from its hydrophobic pocket, TM2a-TM8 detachment and disruption of the H-bond between G42 and A47, can adopt a more flexible arrangement encompassing π-helical, α-helical, and unstructured conformations (see supporting movies). During this first stage of the transition there is a significant free energy increase which correlates with the hydrophobic penalty arising from solvation of apolar intracellular residues (Fig. 6A) as well as disruption of R223-E28 and R223-D21 salt-bridges (Fig. 5D and Fig. S10ABD). Subsequently, partial de-solvation of hydrophobic residues of extra- and intracellular cavities allows the formation of a metastable intermediate (closed intermediate I_A in Fig. 6) which compared to the OF state features ~8 Å translation of TM1-TM6 towards the extracellular side of the membrane (Fig. 6B). The next step entails crossing the highest free energy barrier of the transition (~7 kcal/mol, Fig. 6A), which corresponds to the point in which a few residues in TM1/6 (brown residues in Fig. 5) switch between protein and lipids contacts (Fig. 6A), with the largest contribution provided by the pseudo-symmetric pair F23-F182 highlighted in yellow in the upper panel of Fig. 6B. Namely, upon ~6 Å movement of TM1/6 parallel to the membrane plane, F182 gains contacts with protein hydrophobic residues and loses contacts with lipid tails, whereas the opposite occurs to F23. Near the switching point additional water molecules enter the intracellular Ca^+ cavity and interact with hydrophobic residues therein, which correlates with the formation of a free energy peak (Fig. 6A). These structural changes lead to a second intermediate (intermediate I_B) stabilized by dehydration of the extracellular Ca^+ cavity and formation of Y60-E180 H-bond (Fig. S10C). At this point TM1/6 has nearly reached the same configuration adopted in IF state, whereas TM7a still remains detached from TM3. Complete progression towards the

IF state is finally achieved by structural rearrangements of TM7a from flexible to partially π-helical configurations, associated to close packing of the latter with TM3, formation of G201-A206 H-bond and enclosure of F202 in a hydrophobic pocket. In this last step (IF state in Fig. 6), substantial free energy gain correlates with dehydration of the Na^+ extracellular cavity and formation of K198-E257, K187-D197 salt bridges (Fig. S10C).

In summary, the pathway described above outlines a non-linear transition between OF and IF occluded states, passing through multiple energetic barriers. Starting from the OF state, the protein first partially opens on the intracellular side, adopting intermediate conformations that albeit occluded are not fully packed on either side of the membrane. The protein then fully closes on the extracellular side reaching the IF state (Fig. 6). These structural changes arise from conformational rearrangements of pseudo-symmetric pairs (based on inverted topology repeats) of transmembrane helices; TM1-6 which undergo a large translational movement across the membrane and TM2a-7a that switch from flexible to compact π-helical configurations. Analysis of the contacts of hydrophobic residues with water and protein outlines that, compared to OF and IF states, intermediate configurations are energetically penalized by larger water exposure of the latter residues (see Fig. S10AB and supporting text). Further energetic penalty of these intermediates arises from rupture of salt-bridges and H-bonds that stabilize OF and IF states (Fig. S10CD, left panel of Fig. S10E and supporting text). Remarkably, the binding site region retain the same structure and remains largely water occluded throughout the transition; hence electrostatic interactions therein do not change significantly or provide an energetic contribution to the latter transition (right panel in Fig. S10E and supporting text).

Finally, despite the previously mentioned energetic penalties, the free energy barrier between OF and IF occluded states is surmountable (~7 kcal/mol, Fig. 6; a more global analysis through an Arrhenius plot is provided in Fig. S12, showing consistent results), hence, provided such occluded conformations are attainable, the alternating access transition is energetically feasible.

Ion occupancy determines transport specificity by reshaping the free energy landscape

Our previous study[13] revealed how binding of either three Na^+ ions or one Ca^{2+} ion to NCX_Mj stabilize an outward occluded conformation of the protein, whereas incomplete occupancy or binding to non-transported species (e.g. protonated E213 and E54) lead to protein opening on the extracellular side. Now we have also shown that once the transporter reaches the outward occluded conformation it can also transition to an inward occluded one through a surmountable energetic barrier (Fig. 6A). It remains unclear however whether an analogous occlusion mechanism occurs also for IF conformations of the proteins when ions bind from the intracellular side of the membrane. If confirmed, this bidirectional mechanism of substrate-induced occlusion would completely explain how ions binding control the alternating access transition in agreement with the $3Na^+$:1 Ca^{2+} stoichiometry.

To fully elucidate this question, starting from the derived IF occluded structure of NCX_Mj (for both α-helical π-helical arrangements of TM2a; see Fig. S6 and supporting text), we gradually modified the binding site occupancy through alchemical transformations and MD equilibrations (see methods), following a similar strategy of our previous work[13]. Specifically, we first considered the 3 x Na^+ occupancy state used in the investigation of the OF-to-IF transition (Fig. 1

and Fig. 7), that is three Na^+ ions occupy S_{ext}, S_{Ca} and S_{mid} site and a water molecule is confined in the S_{mid} site, whereas D240 is protonated (Fig. 1C and Fig. 7).
To simulate the Ca^{2+} bound state (1 x Ca^{2+}), we removed the Na^+ ions and added Ca^{2+} at the S_{Ca} site and an extra water molecule at the S_{mid} site to fulfill the coordination geometry proposed in our previous study[13], consisting of Ca^{2+} coordinated with E54 and E213 in a bidentate mode, backbone oxygens of T50 and T209, and two water molecules near the S_{mid} site (Fig. 7). This Ca^{2+} coordination geometry is here confirmed by re-refinement of the previously published crystallographic data at high Ca^{2+} or Sr^{2+} and low Na^+ concentration[13] (see Fig. S13 and supporting text).
To simulate the effect of partial binding site occupancy we also considered two Na^+ ions bound to the protein wherein the S_{int} site is empty (2 x Na^+), namely, having inverted symmetry (based on the rotational axis in Fig. 2A) with respect to the 2 x Na^+ occupancy state previously investigated for the OF state[13] (Fig. 7CD), where the S_{ext} site was empty. Afterwards, we removed the remaining Na^+ ions to simulate the case of an empty binding site (no ions in Fig. 7CD). Additionally, to probe a case with non-transported species, we also performed simulations with two H^+ bound to E54 and E213 respectively (2 x H^+).
Free MD simulations (in the μs time range; Fig. S14 and S15) of the previously mentioned systems show that while 3 x Na^+ and 1 x Ca^{2+} occupancy states retain an inward-occluded conformation during all trajectories, with water molecules excluded from the binding site region, for the other occupancy states, after a few hundred ns MD, water molecules enter the binding pocket leading to protein opening on the intracellular side. These conformational rearrangements are assisted by displacements of TM1 and TM2 which separate from the intracellular portion of TM7 and TM8 (Fig. 7D and Fig. S14, S15). Remarkably, the relative movements of these four transmembrane helices have a noticeable resemblance to those of their pseudo-symmetric counterparts (based

on inverted topology repeats) observed for the extracellular opening transition of the OF state[13] (Fig. 7A and Fig. S16).

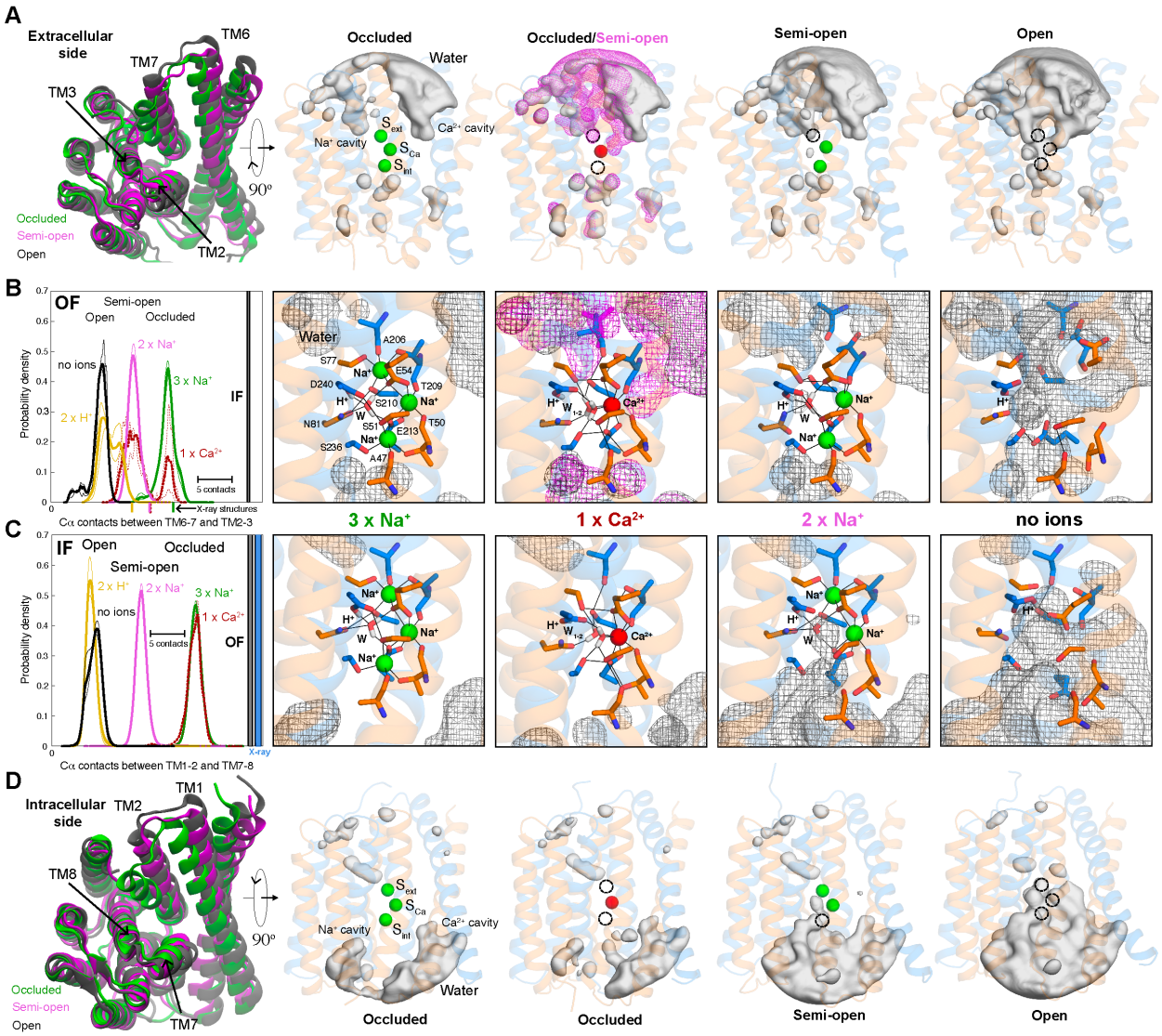

Figure 7. Molecular basis for substrate control of the alternating access transition in the Na^+/Ca^{2+} exchanger (A) From left to right the panel shows representative simulation snapshots of NCX_Mj in cartoon style for OF occluded (green: bound to $3Na^+$ ions), semi-open (magenta: bound to $2Na^+$ ions) and open (dark grey: no ions) conformations overlayed over Cα atoms (except for intracellular loop) and density isosurfaces for water molecules within 12 Å of the ion-binding region (gray volumes), for each ion-occupancy configuration in the OF state. For the Ca^{2+} bound state, density isosurfaces for occluded and semi-open probability peaks (red histogram in panel B) are shown in magenta (mesh) and grey (volume) respectively. Na+ and Ca^{2+} ions are shown as green and red spheres respectively. The two inverted-topology repeats in the transporter structure (transparent cartoons) are colored differently (TM1–5, orange; TM6–10, marine). (B) From left to right the panel shows for each ion-occupancy configuration of the OF state, the probability distribution as function of a descriptor of the degree on extracellular protein opening and close-up views of the ion-binding region for those ion-occupancy states. Key residues involved in Na^+/Ca^{2+} and water coordination (W) are highlighted (sticks, black lines). The water-density maps in B are shown as a gray mesh except for that in the semi-open conformation of the Ca^{2+} bound state which it is shown in magenta. For this state residues that move from their position in the occluded state are also colored in magenta. The thin lines in the probability distributions plot reflect the statistical error calculated through block analysis. The vertical lines below that plot are the position of the X-ray structures of the different occupancy states considered; from left to right pdb entries 5HXH, 5HWY, 5HXR and 5HXE[13]. (C) Same as panel B for the IF state in which the probability distributions are reported as a function of a descriptor of intracellular opening. (D) same as panel A for the IF state.

To more rigorously characterize the conformational dynamics of the ion occupancy states described above, we performed enhanced sampling MD calculations designed to reversibly simulate the transition between inward-occluded and inward-open conformations (see methods). Here we report the results for simulations in which the N-terminal portion of TM2 was set in the α-helical arrangement, which seems slightly more probable that the alternative π-helical one (see Fig. S6). For completeness, we repeated all simulations also for the latter conformation of TM2, which show that the overall trend of the results remains the same (Fig. S17). From these simulations, we quantified for each ion occupancy state the conformational probability as a function of the degree of intracellular opening, measured by the number of Cα contacts between transmembrane pairs TM1-2 and TM7-8 (Fig. 7CD). For comparison, we also reported the same analysis performed on the previously published simulations of the OF state of the transporter, based on the pseudo-symmetric pairs TM6-7 and TM2-3, which are used instead to monitor extracellular opening (Fig. 7AB). The results reveal that either extra- or intracellular ion binding drastically affects the structural dynamics of the transporter, based on a pseudo-symmetric mechanism of ions recognition. When the transporter is bound to either three Na^+ ions or one Ca^{2+} ion, outward-occluded and inward-occluded conformations are highly probable (Fig. 7BC). In the 3 x Na^+ bound state, the occluded conformation is the most probable state and entails a maximally coordinated arrangement of the Na^+ ions by charged and polar residues of the protein (Fig. 7BC), which largely precludes water entrance into the binding site region (Fig. 7). In the 1 x Ca^{2+} bound state (Fig. 7) instead, the effect of Na^+ binding at S_{ext} and S_{int} sites is replaced by a network of hydrogen bonds, which through bridging water molecules located near the S_{mid} site connect S_{ext} and S_{int} residues to the Ca^{2+} coordination shell (Fig. 7BC). The formation of this H-bonds network is only possible in the 1 x Ca^{2+} bound state as, in contrast to Na^+, the former ion (as Sr^{2+}) can achieve coordination of eight[13]. These compensating effects rationalize how the transporter can stabilize the occluded states upon binding to either ion species with different occupancies. Additionally, both 3 x Na^+ and 1 x Ca^{2+} occupancy states feature a pseudo-symmetric arrangement of binding site residues and coordinating ions respect to an axis parallel to the membrane plane (same as that in Fig. 2A), thus explaining how the transporter can stabilize in the same manner both outward- and inward-occluded states (Fig. 7BC).

Provided occluded states are significantly probable, the free energy landscape for the OF to IF conformational switch reported previously shows that the energetic barrier between them is surmountable (~7 kcal/mol; Fig. 6) and hence the alternating access transition is feasible. Furthermore, the binding site region does not contribute significantly to the energetics of this transition as throughout the latter it retains the same geometry and remains occluded from the solvent. This implies that the energetic barrier of the transition between OF and IF occluded states ought to be weekly affected by binding of 1 Ca^{2+} ion rather than 3 Na^+ ions or more generally by variations of binding sites occupancy state, thereby, energetic control of the alternating access process is primarily dictated by the feasibility of the occluded states.

Crucially, our simulations show that when the binding sites are partially Na^+ occupied (2 x Na^+ in Fig. 7) the occluded states are no longer attainable (Fig. 7BC and free energy profiles in Fig. S18), and even more so when the binding sites are empty (no ions in Fig. 7BC) or when they bind non-transported species such as protons (2 x H^+ in Fig. 7BC). This finding demonstrates that the alternating access transition and thus ion translocation across the membrane is only triggered by binding of either 3Na^+ ions or 1Ca^{2+} ion to the protein, as only for those ion occupancy states

occluded conformations become energetically feasible. For the other occupancy states instead, as they entail a significant energetic cost to even reach occluded conformations (at least 4 kcal/mol for the $2Na^+$ state and > 10 kcal/mol for the others. Fig. S18), the alternating access process becomes unfeasible, that is the protein remains effectively locked into either extra- or intracellular open/semi-open conformations. Such more open arrangements of the protein arise from water penetration into the binding pocket (Fig. 7) driven by energetic gain associated to solvation of polar/charged protein residues. When the protein instead gradually binds $3Na^+$ ions or $1Ca^{2+}$ ion and progresses from an open to an occluded arrangement, such solvation effects become progressively offset and eventually outmatched by the formation of ion/protein, protein/protein (H-bonds) and water mediated interactions. Upon reaching one of the occluded states the protein can undergo the alternating access transition and subsequently, transient water density fluctuations and opening motions (e.g., intermediate conformations between occluded and semi-open states), requiring moderate energetic cost (Fig. S18), can trigger ion detachment from the binding sites followed by further protein opening to one side of the membrane, thus leading to ions exchange. The progressive opening of the protein upon substrate release is particularly evident when it gradually loses Na^+ ions following the sequence $3Na^+$, $2Na^+$ and empty binding sites (Fig. 7). Conversely, the Ca^{2+} bound state is by itself more dynamic (Fig. 7 and Fig. S18 with free energy profiles), which being a single ion, facilitates binding/release. This behavior is particularly noticeable in OF conformations where for the Ca^{2+} occupancy state both occluded and semi-open conformations are significantly probable (Fig. 7AB). Specifically, this semi-open arrangement resembles the OF X-ray structure with Ca^{2+} bound (Fig. S13A) and entails an extended water channel that oftentimes reaches out from the Ca^+ cavity to coordinate the Ca^{2+} ion. The latter water coordination is consistent with the presence of extra electron density in that position based on the crystallographic data (Fig. S13A).

In summary, taken together with previous crystallographic and computational analysis, our results explain at the molecular level the mechanism of substrate control of the alternating

access process by the Na^+/Ca^{2+} antiporter and rationalize its exchange function in agreement with the $3Na^+$:1 Ca^{2+} experimental stoichiometry[28, 29, 33, 34].

Simulations and accessibility data point to similar substrate control mechanism in cardiac NCX

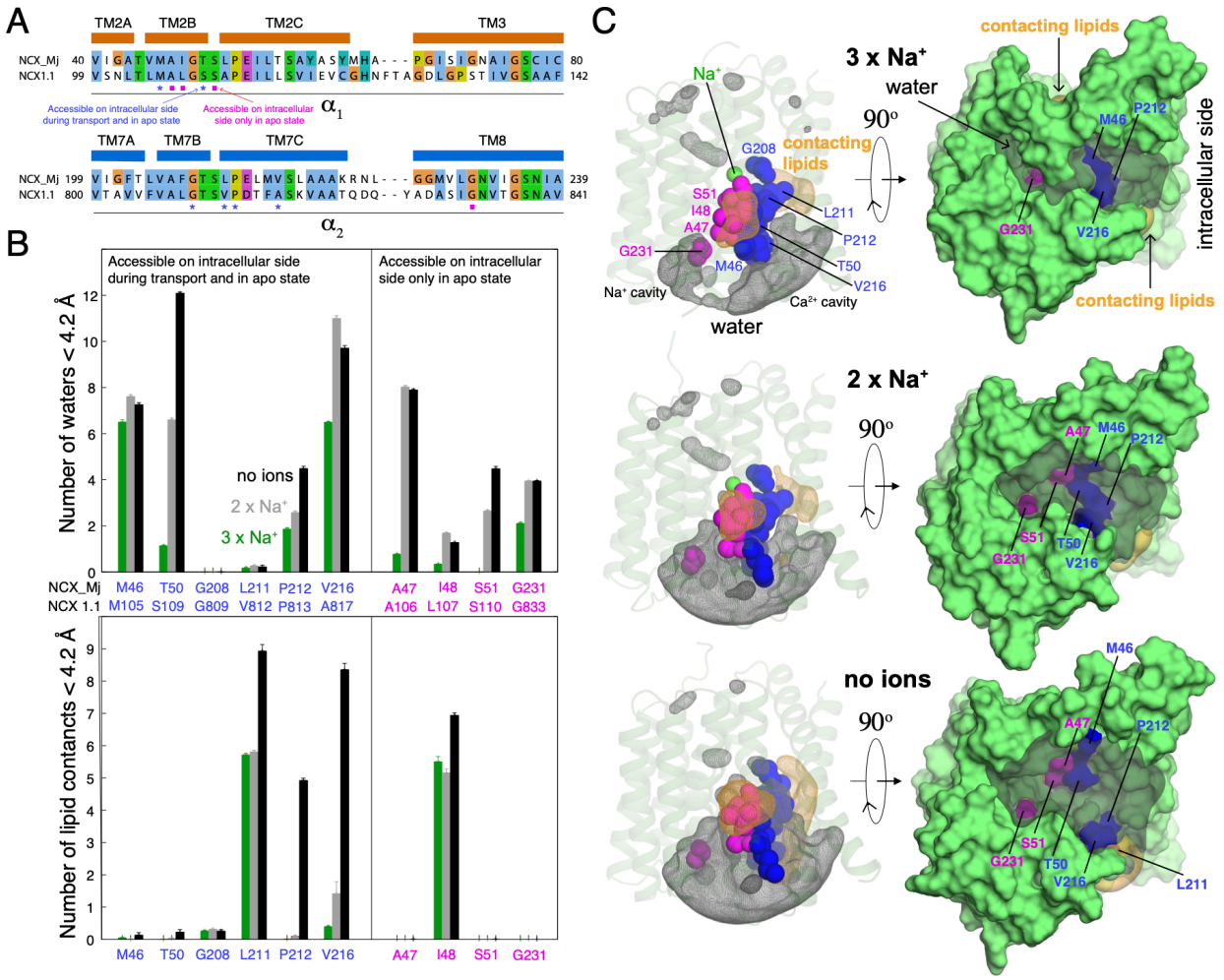

Figure 8. Molecular basis of experimental accessibilities of NCX1.1 based on NCX_Mj simulation models. (A) Sequence alignment of the α-repeats regions of NCX_Mj and NCX1.1. (B) Average number of waters (top) and lipid heavy atoms (bottom) within 4.2 Å of indicated residues (only sidechain) for simulations NCX_Mj in the inward facing state (same as Fig. 7BC) bound to $3Na^+$ (green), $2Na^+$(grey) and no ions (black). Error bars reflects the statistical uncertainty estimated through blocks analysis. The selected residues of NCX_Mj are homologous to those experimentally accessible in NCX1.1 under both transport and apo condition (drawn in blue) or only in apo condition[37] (drawn in magenta). (C) From left to right, density isosurface of waters (within 12 Å of the protein binding sites; gray mesh) and lipids (within 4.2 Å of residues in panel B; bright orange mesh), and surface of the protein intracellular side for the previously mentioned ion-occupancy states. Residues in panel B are reported as blue and magenta spheres (left) or surfaces (right). The same density isosurfaces of waters and lipids are represented as transparent volumes on the right.

The archaebacterial NCX that we studied in this work is considered a reasonably good model of the well-known cardiac NCX, denoted as NCX1.1. Specifically, these two proteins have the same $3Na^+$:1Ca^{2+} exchange stoichiometry[28, 29, 33, 34] and ~20% sequence identity, with the latter rising to ~30% (over 50% similarity) and 75% (100% similarity) in the well-conserved α-repeats

(TMs 2,3,7,8, Fig. 8A) and binding sites regions respectively. Furthermore, recent crosslinking experiments indicate that NCX1.1, as NCX_Mj, comprises 10 transmembrane helices[57]. Hence, it can be expected that they share similar structural features, especially close to the α-repeats[58].

Previous accessibility experiments provide significant information on the structural features of the inward facing state of NCX1.1[37], which can be compared with those inferred from simulations analysis of NCX_Mj. These experimental measurements are based on electrophysiological analysis of cysteine mutations located within the α-repeats [37] (Fig. 8A), wherein the protein mutants were exposed on the cytosolic side to a membrane impermeable covalent reagent and the accessibility was assessed based on the amount of current block after reaction with the cysteine mutated residue. In addition, while a set of experiments was carried out in presence of extracellular Ca^{2+} and intracellular Na^{+}, namely, under transport condition, another set of experiments was performed by substituting Na^{+} with Cs^{+} on the intracellular side, thus representing, non-transport, apo IF condition. Note that the comparative analysis reported here is based only on IF simulation of NCX_Mj, as in the experimental setup the chemical reagent was added only on the cytosolic side of the membrane and OF conformations of NCX_Mj feature negligible intracellular accessibility.

In Fig. 8B we report, for simulations of $3Na^{+}$, $2Na^{+}$ and empty occupancy states, the water and lipid exposures of residues that are equivalent to those reported as accessible in NCX1.1, under both transport as well as apo IF condition (residues marked in blue) or only in apo IF conditions (residues marked in magenta; Fig. 8AB). Overall, residues that are significantly water exposed on the intracellular protein side for all ion-occupancy states, such as M46, P212 and V216 (Fig. 8BC), correlate well with those experimentally accessible in both transport and apo IF condition and also feature fast blocking kinetics[37], underlying easy access of the chemical reagent. Residue T50 pertains to the binding site (Fig. 1C and Fig. 7BC) and is only partially water accessible in the $3Na^{+}$ bound state. Consistently, albeit experimentally accessible, features a somewhat slower blocking kinetics under transport conditions compared to the previously mentioned residues[37]. However, T50 becomes significantly more water exposed in $2Na^{+}$ and empty occupancy states, and accordingly blocking kinetics becomes significantly faster in apo IF conditions[37]. Residues G208 and L211 are detected as experimentally accessible in both transport and non-transport conditions which is not well explained by their poor water exposure from IF simulations (Fig. 8B). This notwithstanding, our analysis shows that L211 is not enclosed in an inaccessible protein pocket as it is lipid exposed in all simulations (Fig. 8BC). Further inspection highlights that, owing to significant membrane deformation near the Ca^{2+} cavity (Fig. S11A), this residue is located near the lipid water intracellular interface, which also seems a preferred location for the methanethiosulfonate moiety of the chemical reagent used in the accessibility experiments[59], hence, it ought to be accessible to the latter in agreement with the experimental observation. Residue G208 is close to L211 but feature negligible water exposure and limited lipids exposure (Fig. 8B), and in fact is reported as having the slowest blocking kinetics under transport condition[37]. Nonetheless, being close to the lipid-water interface, the accessibility of G208 could be affected by cysteine mutation, small structural variations between NCX_Mj and NCX1.1 as well as lipid composition, hence we do not expect strict agreement between simulation and experimental data in this case.

The presence of residues that are experimentally accessible only in apo IF condition, is indicative of a significant structural variation of the protein upon Na^+ release, as predicted for NCX_Mj. Except for G231, the simulations indicate that all these residues are poorly water accessible in the $3Na^+$ bound state, whereas they become more water exposed in partial or empty occupancy states, in agreement with the experimental accessibilities (Fig. 8BC). Further inspection highlights that in the $3Na^+$ bound state G231 resides in a small cavity (Na^+ cavity), which, while water accessible, it might be inaccessible to the larger chemical reagent used in the experiments, which might explain why the according to the latter G231 is inaccessible under transport conditions. In addition, the size of the Na^+ intracellular cavity might vary between NCX_Mj and NCX1.1. Nonetheless, the simulations suggest that such cavity becomes significantly larger and much more water accessible upon Na^+ unbinding (Fig. 8C), which well correlates with the experimental observations. Interestingly, among these residues I48 is lipids exposed in all ion occupancy states (Fig. 8B), however, its position is not particularly close or connected with the water-lipid interface hence it's accessibility to the chemical reagent is expected to correlate more with water rather than lipid exposure. Consistently with the experiments, the water accessibility of I48 become significant only in $2Na^+$ or empty occupancy states (Fig. 8BC).
Overall, this analysis provides significant evidence that the inward-facing states of NCX1.1 and NCX_Mj share similar structural features and that both proteins undergo an analogous substrate-induced conformational change from an open to an occluded conformation.

Discussion

Selective and active secondary transport requires that the alternating access mechanism of the membrane transporter[3, 4, 8, 9] is only triggered by proper substrate occupancy states. For Na^+/Ca^{2+} exchangers, for example, binding of either three Na^+ or one Ca^{2+} induces a conformational switch between outward and inward-facing conformations that, depending on the ion electrochemical gradients, leads to transport of those ions in the opposite direction[26, 27, 33] (Fig. 9). Furthermore, to effectively transport the substrates, and prevent dissipation of the driving force, some of the protein conformations should not be energetically feasible. However, it is not clear the molecular mechanism that forbid states, as for example, a continuous open pore. Here, we elucidated the molecular basis of this functional mechanism using quantitative molecular simulation approaches coupled to previous HDX-MS and accessibility measurements.
The simulations reported here capture different conformational states of a prokaryotic Na^+/Ca^{2+} exchanger (NCX_Mj), including previously unknown inward-facing conformations and intermediates of the alternating access transition. They also quantify the energetic stability of each of these states (Fig. 1,2), the energetic barriers for the transitions between them (Fig. 6) and how these are reshaped by ion-binding events (Fig. 7). Altogether, these computational data reveal the interplay between ion binding and alternating-access conformational change in this protein. The relevance of the structural computational models predicted here (with possible limitations of the simulation energy function) is supported by the fact that a diverse set of available outward-facing X-ray structures[13, 35] correspond to energetically accessible

conformations of the calculated free energy landscapes (Fig. 1,2 and 7). This is also true for conformations that were not specifically used in the simulations (Fig. 7)[13] since all simulations are started from one structure (pdb entry 3V5U[35]). Additionally, we explicitly validated the predicted inward-facing states comparing with the available accessibility data[37, 42] (Fig. 4 and Fig. 8) and performing ensemble reweighting based on previous HDX-MS measurements [42] (Fig. 4).

The results demonstrate that, similarly to an enzyme, the transporter lowers the activation barrier for translocation through an induced-fit mechanism triggered by the binding of appropriate substrates. Namely, binding of either three Na^+ or one Ca^{2+} to the transporter induces the formation of intermediate occluded conformations (Fig. 7 and Fig. 9) of the protein, that ultimately open an energetically permitted pathway to the alternating access transition (Fig. 6 and Fig. 9). As shown by our computational analysis (Fig. 6 and Fig. 7) and its comparison with previous accessibility data[24] (Fig. 8), this occlusion mechanism provides a kinetic control of the antiport function that explains the $3Na^+$:$1Ca^{2+}$ stoichiometry reported experimentally[28, 29, 33, 34]. Furthermore, it also explains transport selectivity; occluded states are unattainable when the protein binds to protons. This rationalizes how Na^+/Ca^{2+} antiporters do not catalyze Ca^{2+}/H^+ exchange[35] (Fig. 7 and Fig. 9) although under low pH the binding site can be occupied by protons. We posit that a similar mechanism applies to other divalent cations, as Cd^{2+} and Mn^{2+}, that bind to the transporter[35] but act as non-competitive inhibitors[35, 60, 61]. Based on the observation that similar substrate-induced conformational changes have been also captured in experimental structures of other secondary transporters, regardless of their particular type of alternating access mechanism (as for example Mhp1 [62], vSGLT[63, 64], LeuT[65-68], LacY[69, 70] and Glt_{Ph}[71]), we envisage that the proposed mechanism of selective occlusion provides a general principle for kinetic control of function in these proteins[3].

For the Na^+/Ca^{2+} exchanger studied here, the mechanism of ions-induced extracellular occlusion has been characterized by our previous simulation (which we re-analyzed here) and crystallographic data[13]. We showed that the occlusion arises from extracellular packing of TM6-TM7 against TM2-TM3 (Fig. 7A). The new simulations performed here instead reveal the molecular details of the conformational switch between outward-occluded and inward-occluded states (in the 3 x Na^+ occupancy state) as well as how ions release from the latter promotes intracellular opening. Our data show that the inward-to-outward transition occurs through a new type of alternating access mechanism. This involves sliding of the TM1-TM6 bundle by ~1nm across the membrane coupled to structural rearrangements of TM2a-TM7a (Fig. 2, Fig. 3AB and Fig. 6). The ions, instead, remain bound at the center of the protein and shielded from water (Fig. 2 and Fig. 6). These movements of topologically inverted helix pairs are consonant with those inferred from the internal pseudo-symmetry of the protein[5, 35] and are also in line with the X-ray structures of inward-facing Ca^{2+}/H^+ exchangers[38-40] (Fig. 3CD). Hence, they support a conserved alternating access mechanism in the cation/Ca^{2+} superfamily[72]. We have also shown that during this transition a complementary set of hydrophobic, hydrophilic, and lipid-mediated interactions alternatively form and disrupt at the two sides of membrane (Fig. 5 and Fig. 6). Previous mutational analysis highlighted how some of the residues involved in those interactions are critical for protein function (T57, F202, G76, D197) and determine the apparent intracellular and extracellular ions affinities (G42, G201, V205, G231, G235)[47, 48]. In addition, these residues are partially conserved across inverted topological repeats (Fig. S1), which explains how the

internal pseudo-symmetry of the protein lays the groundwork for generating two stable alternating access conformations[3, 5, 8] (Fig. 1D). During the conformational cycle, the interchange of the previously mentioned interactions leads to crossing metastable closed intermediates and multiple energetic barriers (Fig. 6), but no structural changes occur within the protein binding site, and no leaking pore states are ever formed (Fig. 1D). Despite the barriers are surmountable (6-7 kcal/mol; Fig. 6), they likely determine the low turnover rate of NCX_Mj (0.5 s^{-1}) [47] which compared to mammalian NCX orthologs is over 1000 slower[26, 73, 74]. Previous work showed that replacement of the protein binding site of NCX_Mj to match that of the cardiac NCX and changes in the lipid composition do not fill this gap in the turnover rates[75]. We believe that the cardiac NCX may stabilize the closed intermediates minima identified here, through interactions not at the binding site. This type of halfway intermediates between outward and inward facing conformations has been captured in X-ray structures of different secondary transporters[10-12].

The last set of simulations that we performed complete the structural information on the conformational cycle of NCX_Mj. Namely, starting from the inward-occluded state, predicted and validated here, we showed how partial ion occupancies or different ion types leads to intracellular opening mediated by helical movements that are pseudo-symmetrical respect to those observed for extracellular opening (TM1-TM2 detaches from TM7-TM8; Fig. 7CD). These structural changes are compatible with HDX-MS experiments that report reduced deuterium uptake levels upon Na^+ and Ca^{2+} binding for a mutant (5L6-8) of NCX_Mj that favors inward facing conformations[42]. Furthermore, they are also consistent with previous accessibility data on the cardiac NCX[37] which outlines how this occlusion mechanism is common in prokaryotic and mammalian NCX (Fig. 8).

In summary, taken together with previous computational and structural studies, our work explains, at the molecular level, previous functional, biochemical, and biophysical data on Na^+/Ca^{2+} exchangers and establishes the molecular basis for selective and active transport in these proteins.

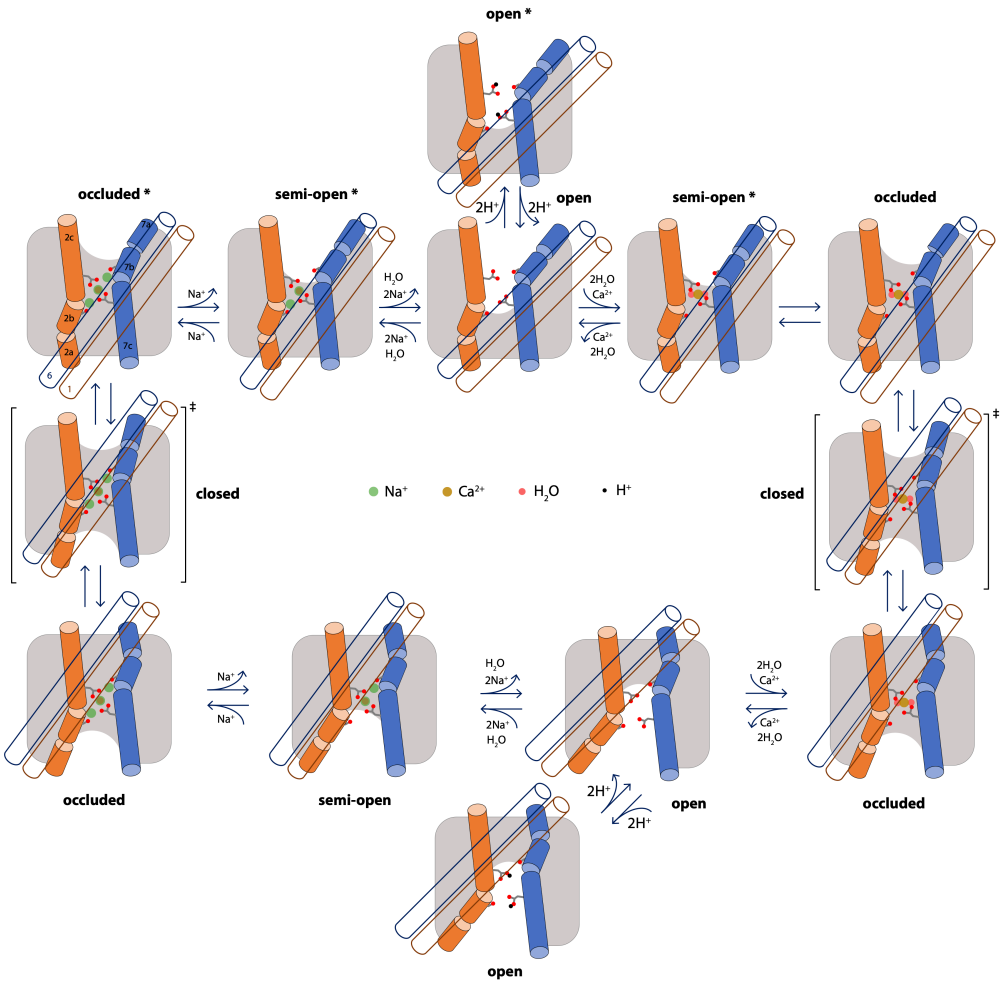

Figure 9. Schematics of the proposed alternating access mechanism of the Na^+/Ca^{2+} exchanger. The carbonyl groups of A47 (on TM2b) and A206 (on TM7b), and the side chains of E54 (on TM2c) and E213 (on TM7c) are highlighted. The blue and brown empty cylinders denote the sliding helices TM1 and TM6. The orange and marine cylinders represent TM2 and TM7 respectively. States and connectivity have been deduced from the calculated free-energy landscapes. Asterisks mark the states determined also by X-ray crystallography[13, 35]; from left to right pdb entries 5HXE (or 3V5U), 5HWY (or 5HWX), 5HXH and 5HXR.

Methods

Repeat-swap model of the inward facing conformation of NCX_Mj

The reaction coordinates that were used to enhance the simulations sampling (see section below) are based on the OF X-ray structure of NCX_Mj[35] and on an IF model that was derived using the repeat-swapping technique[76]. Namely, the IF model was derived according to the structural relationship between the two inverted topological repeats of NCX-Mj (Fig. S1AB). The concept is that, despite the structural and sequence similarities, each repeat adopts a different conformation (Fig. S1B), hence indicating that alternating access arises from a concerted conformational switch of both repeats[5, 8]. Thus, we generated a template for modelling the IF conformation by swapping the residue numbers of the two repeats in the X-ray structure (Fig. S1AB), with the specific sequence alignment provided in Fig. S1C. Our previous work outlined that

when the protein is fully bound with 3 Na^+ ions, the binding site adopts a symmetric coordination with respect to an axis parallel to the membrane plane[13, 36]. Hence, it can be expected that the binding site geometry remains mostly unaltered during the OF-IF conformational change and was preserved by restraining the distances between Na^+ and coordinating oxygens as well as oxygen-oxygen distances. Following an established protocol[76] we generated 250 IF models using MODELLER[77] v9.15 and selected one of them for further refinement. In particular, we repositioned the side chains of scaffold regions according to the X-ray structure (Fig. S1A) and we corrected sidechain rotamers using SCWRL4[78]. The model was then energy minimized, embedded in a solvated POPC bilayer using GRIFFIN[79] and equilibrated for 800 ns at constant temperature (298 K), pressure (1 atm) and membrane surface area (~69 $Å^2$ per lipid). The MD simulation were carried out with NAMD v 2.12[80] using the CHARMM27/CMAP force field[81, 82] and the same setup of our previous work[13]. The MD equilibration involves a set of stages in which first position restraints and then RMSD restraints (where the protein is allowed to freely tumble) are gradually removed on protein sidechain and backbone atoms. Thereafter we performed additional 3 μs MD simulation without any restraint (Fig. 3 and Fig. S7).

Enhanced Sampling MD simulations of the OF-to-IF transition of NCX_Mj

The MD simulations used to calculate the free energy landscapes of the alternating access transition are based on bias exchange metadynamics calculations (BE)[44] carried out with GROMACS 4.5.5/PLUMED[83-85] at constant temperature (298) and pressure (1 bar). All simulations used the CHARMM 36m[86] and CHARMM36[87] force fields for protein and lipids respectively, with a modified version of the Lennard-Jones R_{min} parameter for the Na^+-carboxylate interaction[36]. Electrostatic interactions were evaluated with PME using a real-space cutoff of 9 Å; the same cutoff distance was used for Lennard-Jones interactions. The initial atomic coordinates correspond to an equilibrated configuration of the 3 x Na^+ bound X-ray structure[35, 36], obtained from previous MD calculations[13]. To limit the number of possible protein conformation to be sampled and converged, we removed the intracellular loop between residues A148 and N157 (dotted loop in Fig. 1A), which is not critical for the transport function[47]. This initial configuration was equilibrated in three stages: two MD simulations with position restraints on protein heavy atoms; the first (30 ns) at constant surface area and the second (40 ns) at constant pressure. This was followed by 60 ns simulation without any restraints. The BE calculations consist of a set of enhanced sampling simulations (or replicas) that exchange coordinates (every 10-20 ps) according to a Metropolis criterion[44]. To reduce the energetic barrier of alternating access protein conformational changes, each replica entails a metadynamics bias potential[88, 89] applied on small subset of the reaction coordinates. For such complex conformational changes it is difficult to derive a single optimal reaction coordinate[17], as this would require preliminary detailed knowledge of the inward facing conformation of the transporter as well as of the most likely intermediate conformations of the alternating access transition. Therefore, we opted for a wide set of reaction coordinates (18 in total), none of the which is necessarily optimal, but coupled together through the BE technique are expected to facilitate the sampling of all the relevant outward-to-inward transition pathways. The most probable protein conformations are then extracted post-hoc from simulation analysis (see below).

Based on a repeat-swap model[5, 8] of the IF state (IF-rs), we selected a set of reaction coordinates (ξ_i) that measure the linear progress of a given configuration from OF (equilibrated 3 x Na^+ bound X-ray structure[35, 36]) to IF-rs conformations, in the form of a path collective variable[90]:

$$\xi_i(t) = \frac{exp\{-\lambda d_1(t)\} + 2exp\{-\lambda d_2(t)\}}{exp\{-\lambda d_1(t)\} + exp\{-\lambda d_2(t)\}} \quad (1).$$

Where $d_1(t)$, $d_2(t)$ are the mean square displacements (MSDs) of the current configuration (at time t) relative to either OF or IF-rs conformations, respectively. The smoothing parameter λ is proportional to the inverse of the MSD between these two reference structures (table S1). According to the definition of ξ_i (eq. 1), configurations that are much closer to the X-ray structure than to the IF-rs model correspond to $\xi_i \sim 1$, conversely, $\xi_i \sim 2$ in the opposite case. All other configurations result in intermediate values of ξ_i comprised between one and two.

A set of 18 reaction coordinates of this type was generated by defining each path collective variable in reference to a particular protein region, selected among protein backbone, loop/helix fragments and residues sidechains facing intracellular and/or extracellular sides of the membrane (Fig. S2). Each replica of the BE simulations, except for the unbiased ones, entails a metadynamics bias potential applied on two of the previously mentioned path collective variables, with the combinations reported in table S1. We also applied boundary potentials to maintain the Na^+ and the water molecule bound to the respective sites (Fig. 1C). For Na^+ the potential was applied on the following variable:

$$\xi_C(t) = \sum_k \frac{1 - \left(\frac{r_k}{r_0}\right)^8}{1 - \left(\frac{r_k}{r_0}\right)^{10}} \quad (2),$$

where r_k is the distance between ions and coordinating oxygen atoms and $r_0 = 0.24$ nm. For this variable we set lower values of $\xi_0 = 4.3$ for Na^+ ions bound to S_{int} and S_{ext} sites (coordinated to 5 oxygens) and $\xi_0 = 4.75$ for the one bound to S_{Ca} (coordinated to 6 oxygens; Fig. 1C), using a potential of the form $k_C(\xi_C(t) - \xi_0)^4$, applied when $\xi_C(t) < \xi_0$ and for which $k_C = 1000$ kJ/mol. The water molecule in the binding site (Fig. 1C) was confined with half harmonic potential, $k_d(r(t) - r_0)^2$, on the distances (r) between the water oxygen and the C_γ atoms of N81 and D240 respectively. This potential was set with $k_d = 10000$ kJ/(mol nm^2) and applied when either of the distances is larger than $r_0 = 0.46$ nm .

For the BE calculations, we carried out an initial equilibration stage of 1 μs (for each replica) using 32 replicas (31 biases replicas and one unbiased). During this stage, each replica reached uniform sampling in the space of the biased reaction coordinates, and seven continuous trajectories (reconstructed post-hoc from the exchanging replicas) visited independently the inward facing state. This state was sampled by the unbiased replica after 850 ns, confirming that it lies on a low free energy region of the landscape. After exploring the relevant protein conformations, we aimed to converge the sampling by doubling the number of replicas to 64 (table S1) and continuing each simulation for other 200 ns, with a total simulation time of 45 μs. The free energy landscapes were derived using the sampling obtained with 64 replicas.

Analysis based on free energy landscapes of the alternating access transition of NCX_Mj

To calculate the free energy map of Fig. 1D, we analyzed the sampling of 12 BE replicas; two unbiased, six with a bias applied on ξ_6 and ξ_{13} and four biased along ξ_{16} and ξ_{17} (Fig. S2 and table S1). The first two of these variables describe open and closing of either intracellular (ξ_6) or extracellular (ξ_{13}) protein regions, whereas the last two detect the conformational rearrangements around either Ca^{2+} (ξ_{16}) or Na^{+} cavities (ξ_{17}; see also Fig. 2A). We derived the free energy across those variables by estimating the free energy derivatives (mean forces) on each point of a four-dimensional grid (dividing the space in 60 bins along each direction), using the force-correction analysis method (FCAM)[41]. The free energy was obtained by mean forces integration, using a kinetic Monte Carlo approach[41]. The free energy map in Fig. 1D was obtained by integrating the four-dimensional (4D) probability distribution (Boltzmann distribution based on the 4D free energy landscape) on ξ_{16} and ξ_{17} to obtain the free energy as a function of ξ_6 and ξ_{13} (Fig. 1D).

Water/protein/lipid densities and other structural quantities in Fig. 2 and Fig. 5 are based on configurations that are within 1 kcal/mol of either OF or IF free energy minima in Fig. 1D. These configurations were re-sampled from the 12 BE simulations replicas mentioned above, according to a Monte Carlo approach, so that their probability is proportional to the Boltzmann weight dictated by the free energy as a function of ξ_6, ξ_{13}, ξ_{16} and ξ_{17}. Pairwise RMSD distributions in Fig. 3 are based on the same Monte Carlo approach, with a threshold of 2 kcal/mol from either OF or IF free energy minima.

The *X* direction in Fig. 2BC is defined by the axis connecting the centers of two groups of Cα protein atoms; the first group comprises residue ranges 102-108 and 112-118 (pertaining to TM4) whereas the second group entails residues 258-264 and 268-274 (pertaining to TM9). The *Z* direction is defined similarly with the first group of Cα atoms comprising residue ranges 102-108 and 268-274 (intracellular portions of TM4 and TM9) whereas the second group entails residues 112-118 and 258-264 (extracellular portions of TM4 and TM9). The position of TM1-TM6 projected along those axes (Fig. 2C and associated caption) is defined by the center of Cα atoms of residue ranges 1-33 (TM1) and 160-192 (TM6). The free energy map of the TM1-TM6 center projected along *X* and *Z* directions was calculated from the weighted histogram as a function of those variables, based on the sampling of the previously mentioned 12 BE replicas. To ensure unbiased sampling, the weight of each simulation frame, i, was set as $\exp\{-F(\boldsymbol{\xi}^{\alpha(i)})/k_{\mathrm{B}}T\}/N_{\alpha(i)}$, where $F(\boldsymbol{\xi}^{\alpha(i)})$ is the free energy as a function of ξ_6, ξ_{13}, ξ_{16} and ξ_{17}, $\alpha(i)$ is the 4D bin assigned to frame i and $N_{\alpha(i)}$ is the total number of frames in that bin[41]. The map in Fig. 2E was calculated similarly from the weighted histogram of the O-N distances between residues G42-A47 and G201-A206.

The details of the ensemble reweighting approach to couple the free energy calculations with the HDX-MS experiments (Fig. 4) are provided in the supporting information (see supporting text).

The minimum free energy path of Fig. 6 reflects the most likely pathway (at a low temperature of 10K) from OF to IF conformations across a free energy landscape as a function eight reaction coordinates: ξ_6, ξ_7, ξ_8, ξ_{13}, ξ_{14}, ξ_{15}, ξ_{16}, ξ_{17} (Fig. S2). This free energy landscape was obtained calculating the mean forces on an eight-dimensional grid (dividing the space in 40 bins along each direction), as described previously, and using the sampling of 20 BE replicas: two unbiased, and the others biased on two among the eight reaction coordinates mentioned previously (table S1).

Remarkably, the free energy map as a function of ξ_6 and ξ_{13} obtained from the eight-dimensional (8D) landscape (by integration of the 8D probability density) matches within the uncertainty that derived from the 4D landscape mentioned above (Fig. S19), underlying the accuracy and consistency between the two high-dimensional landscapes. The most likely pathway from OF to IF conformations across the eight-dimensional space was calculated by maximizing the pathway probability using a simulated annealing approach as reported in a previous work[41]. To ensure that the calculated pathway describes a continuous set of transitions, here we considered that two neighboring bins of the 8D grid are connected only if transitions between them are observed during continuous trajectories.

Re-refinement of $Ca^{2+}$and Sr^{2+} bound X-ray structures

For re-refinement of outward-facing X-ray structures of NCX_Mj in the Ca^{2+} and Sr^{2+} bound states we used the electron densities downloaded from the protein data bank (pdb entries 5HXR and 5HXS[13]). Model building was completed with COOT[91], and structure refinement was carried out with PHENIX[92].

Conventional molecular dynamics (MD) simulations

Conventional (i.e. not enhanced) MD simulations were carried out with GROMACS2018 and GROMACS 4.5.5/PLUMED[83-85, 93] (the latter was used when confining potentials were applied) using the same force field and simulation parameters of the enhanced sampling calculations reported above. A set of MD simulations was carried out starting from OF and IF configurations (three for each state) extracted from the enhanced sampling calculations. These simulations were run for 12.6 μs in total (6 μs and 6.6 μs for OF and IF simulations respectively, Fig. S3).
Another set of MD simulations was carried out for different ion-occupancy states of NCX_Mj in the IF state. The initial configuration of the two-Na^+ state was generated from the 3Na^+ bound IF conformation extracted from the enhanced sampling calculations by displacing the Na^+ ion at S_{int}. This was done through a slow alchemical transformation that annihilates the bound ion (during 40 ns simulation). A Cl^- ion in the bulk solution was concurrently annihilated to maintain neutrality. An initial configuration for the apo state (i.e., no ions in Fig. 7CD) was derived from the equilibrated 2 x Na^+ state by annihilating (during 40 ns simulation) the Na^+ ions from the binding sites concurrently with two Cl^- ions in the bulk solution. For the two-H^+ state, an initial configuration was generated from the 3Na^+ bound IF state by gradually annihilating (during 100 ns simulation) the Na^+ ions from the binding sites (plus a Cl^- ion in the bulk) and creating protonated E54 and E213 side chains. The initial configuration of the Ca^{2+} bound state was generated from the 3x Na^+ bound IF state (same as above), by removing bound Na^+ ions and introducing a Ca^{2+} ion at the S_{Ca} site. The water molecule at the S_{mid} site was also removed and replaced with two water molecules coordinating the Ca^{2+} ion to fulfill the coordination geometry of the re-refined X-ray structure with high Ca^{2+} and low Na^+ concentration (Fig. S13A). The obtained structure was energy minimized and relaxed during 10 ns MD simulation with positions restraints on all protein heavy atoms except binding site residues (Fig. 1C). The Ca^{2+} ion and coordinating water molecules were also subject to position restraints at this stage. For all ion

occupancy states, after obtaining initial configurations we performed ~1μs MD equilibration (Fig. S14 and S15). For the 1 x Ca^{2+} bound state we applied a boundary potential during the simulation to maintain the Ca^{2+} bound to the S_{Ca} site. This potential was applied on the coordination variable defined by eq. 2 in which r_k is the distance between Ca^{2+} and a coordinating oxygen atom, and $r_0 = 0.3$ nm. For this variable we set a lower value of $\xi_0 = 7.4$ using a potential of the form $k_C(\xi_C(t) - \xi_0)^2$, applied when $\xi_C(t) < \xi_0$ and for which $k_C = 400$ kJ/mol. The two water molecules in the binding site (Fig. 7C) were also confined with a half harmonic potential, $k_d(r(t) - r_0)^4$, on the distances (r) between the C_γ atoms of either N81 or D240 residues with the oxygen atom of the adjacent water molecule. For this potential $r_0 = 0.41$ nm and $k_d = 10000000$ kJ/(mol nm^4). An additional simulation of 730 ns shows that the initial Ca^{2+} coordination geometry (and the overall protein conformation) is retained also in absence of confining potentials (data not shown).
The previously mentioned simulations were replicated for both IF substates of NCX_Mj (IF_α and IF_π in Fig. S6 and supporting text) in which TM2a is ether in α- or π-helical conformation and the loop between TM1 and TM2 is either extended or compact (Fig. S14 and Fig. S15). The equilibrated structures of each ion-occupancy state were used as initial configuration for enhanced sampling calculations (see below).

Enhanced Sampling MD simulations of ions-induced intracellular occlusion of NCX_Mj

The MD simulations of the transition between inward-open and inward-occluded states of NCX_Mj are also based on BE calculations that use the same software and simulation specifications of those reported above. The choice of the collective variables is based on the analysis of the unbiased MD trajectories, following an analogous protocol of our previous study[13]. Specifically, to enhance the reversible entrance and exit of water molecules from the intracellular side of the membrane into either the S_{int} or the S_{Ca} binding sites, we used the following collective variable:

$$\xi_{int,Ca}(t) = \frac{\beta}{ln \sum_i exp\{\beta / r_i(t)\}} \quad (3),$$

where $r_i(t)$ denotes the time-dependent distance between the oxygen atom of each water molecule in the system, i , and the center of the binding respective site considered (ξ_{int} for S_{int}, ξ_{Ca} for S_{Ca}), and β is 10 nm. When the binding site was occupied, the ion was used to define its center. If the site was empty, its center was defined as the center of mass of the oxygen atoms coordinating the ion if bound. Bound water molecules at or near S_{mid} (coordinating the Na^+ or Ca^{2+} ions) were not considered.
To control reversible intracellular opening and closing, we used two path-collective variables. The first one, $\xi_{TM1,2-7}$, is defined according to eq. 1 and describes the movement of intracellular portions of TM1 (residues 18-26) and TM2 (residues 45-50) relative to that of TM7 (residues 211-217). In this case, the terms $d_1(t)$, $d_2(t)$ in eq. 1 describe the MSDs (defined with Cα atoms of the selected residues of TM1, TM2 and TM7) of the current configuration relative to either intracellularly closed or open conformations, respectively. Representative closed and open conformations were extracted from MD simulations of 1 x Ca^{2+} and apo occupancy states, respectively, and $\lambda = 20$ nm^{-2}. The second path-collective variable describes instead relative

opening/closing movements of intracellular portions of TM2 (residues 45-50) and TM8 (residues 232-236), and is defined with three reference states:

$$\xi_{TM2-8}(t) = \frac{exp\{-\lambda\, d_1(t)\} + 2exp\{-\lambda\, d_2(t)\} + 3exp\{-\lambda\, d_3(t)\}}{exp\{-\lambda\, d_1(t)\} + exp\{-\lambda\, d_2(t)\} + exp\{-\lambda\, d_3(t)\}} \quad (4).$$

Where $d_1(t)$, $d_2(t)$ and $d_3(t)$ are the MSDs (defined with backbone atoms of the selected residues of TM2 and TM8) of the current configuration with respect to progressively more open reference structures. These structures were selected from MD simulations of 1 x Ca^{2+} (d_1) and 2 x Na^+ occupancy states (d_2 and d_3), and $\lambda = 200$ nm^{-2}. Note that in the definition of these path-collective variables we omitted the terminal portions of the TM regions.

To maintain ions and waters bound to the respective sites we used same the boundary potentials described above. In particular, the 2 x Na^+ state entails the same restraining potentials of the 3 x Na^+ state for Na^+ ions and water molecules except for the S_{int} site which is empty. No boundary potentials were applied for simulations of 2 x H^+ and no ions states.

The BE simulations entail 16 replicas; 15 with a well-tempered metadynamics[94] biasing potential applied on different subsets of collective variables, as specified in table S3, and one unbiased replica. The total simulation time is 300 ns for each replica, in which the last 100 ns were used for analysis (i.e., after equilibration).

To assess whether the boundary potentials on the ions affect the probability of intracellular opening of the 3 x Na^+ occupancy state (which has the largest number of restraints), we replicated the BE simulations by removing residue A47 in the definition of the coordination variable (see eq. 2) used to define the boundary potential applied to the Na^+ ion bound at S_{int} (and we set its lower limit to 3.45; see above). This change ought to increase the probability of A47- Na^+ detachment, thus facilitating intracellular opening, however, the results show that it does not alter the probability of intracellular opening (Fig. S20).

The previously mentioned BE simulations were replicated for both IF_α and IF_π substates (see Fig. S6 and supporting text). Data reported in Fig. 7CD are based on simulations of the IF_α substate, the analogous results for the IF_π substate are provided in Fig. S17.

Protein conformational probabilities of the different ion occupancy states of NCX_Mj

To translate the BE simulation data into free energy landscapes or conformational probabilities, we identified two pseudo-symmetric structural descriptors that are both intuitive and well-represent closing/opening motions of IF and OF states of NCX_Mj upon ions binding/release. These are defined by the number of Cα contacts between transmembrane pairs: intracellular portions of TM1-TM2/TM7-TM8 for simulations of the IF state of the protein and extracellular portions of TM6-TM7/TM2-TM3 for the OF state. For the latter state we re-analyzed our previously published simulations[13]. The number of Cα contacts is defined by:

$$S_C(t) = \sum_{ij} \frac{1 - \left(\frac{r_{ij}(t)}{r_0}\right)^4}{1 - \left(\frac{r_{ij}(t)}{r_0}\right)^8} \quad (5),$$

where $r_0 = 0.7$ nm and r_{ij} denotes the Cα–Cα distance between residue i and j. For simulations of the IF state, the indexes i and j comprise intracellular facing residues of TM1-TM2 (residue

numbers 17, 20, 21, 24, 25, 42, 43, 46, 47, 48, 50) and TM7-TM8 (residue numbers 211, 212, 213, 215, 216, 219, 220, 231, 232, 235, 236), respectively. For simulations of the OF state, i and j are residue numbers corresponding to extracellular portions of TM6-TM7 (176, 179, 180, 183, 184, 201, 202, 205, 206, 207, 209) and TM2-TM3 (52, 53, 54, 56, 57, 60, 61, 72, 73, 76, 77), respectively.

For each simulation set we derived the unbiased probability as a function of S_C (Fig. 7BC) as the weighted histogram across BE simulation configurations, in which the weight encompasses the free energy as a function of the reaction coordinates that are biased during the simulation. The free energy was derived from the calculation of the mean forces[41] as detailed in a previous section (see *Free energy landscapes of the alternating access transition of NCX_Mj*). For Ca^{2+} occupancy states, histograms were corrected on account of the excess amount of charge transferred from the ion to the protein[13] (based on which Ca^{2+} has a reduced charge of 1.8 and coordinating residues/molecules a proportionally increased charge). To do so, we multiplied the weight of each configuration, i, by a reweighing factor given by:

$$W_i = exp\left\{-\frac{U_i^C - U_i}{k_\mathrm{B}T}\right\} \qquad (6),$$

where the term $U_i^C - U_i$ is the difference between the potential-energy functions with modified and conventional charges, respectively.

Acknowledgements

We are grateful to Emel Ficici for her help in the derivation of the inward facing homology model of NCX_Mj based on inverted topological repeats. We are grateful to Vanessa Leone for suggestions and reading the manuscript. This work was funded by the Division of Intramural Research of the National Heart, Lung and Blood Institute (NHLBI), National Institutes of Health (USA). Most of the computational resources were provided by the NIH high-performance computing facility Biowulf.

Author contributions

F.M. and J.F.G. conceptualized research. F.M. designed and conducted research. F.M. analyzed and interpreted data. F.M. and J.F.G. wrote the manuscript. J.F.G. provided funding acquisition.

Declaration of interests

The authors declare no competing interests

References

1. Noble, D., *The initiation of the heart beat*, ed. C. Press. 1979, Oxford.
2. Bers, D.M., *Calcium cycling and signaling in cardiac myocytes.* Annu Rev Physiol, 2008. **70**: p. 23-49.
3. Beckstein, O. and F. Naughton, *General principles of secondary active transporter function.* Biophys Rev, 2022. **3**(1): p. 011307.
4. Jardetzky, O., *Simple allosteric model for membrane pumps.* Nature, 1966. **211**(5052): p. 969-70.
5. Forrest, L.R., et al., *Mechanism for alternating access in neurotransmitter transporters.* Proc Natl Acad Sci U S A, 2008. **105**(30): p. 10338-43.
6. Forrest, L.R., *Structural biology. (Pseudo-)symmetrical transport.* Science, 2013. **339**(6118): p. 399-401.
7. Forrest, L.R., *Structural Symmetry in Membrane Proteins.* Annu Rev Biophys, 2015. **44**: p. 311-37.
8. Forrest, L.R., R. Kramer, and C. Ziegler, *The structural basis of secondary active transport mechanisms.* Biochim Biophys Acta, 2011. **1807**(2): p. 167-88.
9. Drew, D. and O. Boudker, *Shared Molecular Mechanisms of Membrane Transporters.* Annu Rev Biochem, 2016. **85**: p. 543-72.
10. Yin, Y., et al., *Structure of the multidrug transporter EmrD from Escherichia coli.* Science, 2006. **312**(5774): p. 741-4.
11. Perez, C., et al., *Alternating-access mechanism in conformationally asymmetric trimers of the betaine transporter BetP.* Nature, 2012. **490**(7418): p. 126-30.
12. Hirschi, M., Z.L. Johnson, and S.Y. Lee, *Visualizing multistep elevator-like transitions of a nucleoside transporter.* Nature, 2017. **545**(7652): p. 66-70.
13. Liao, J., et al., *Mechanism of extracellular ion exchange and binding-site occlusion in a sodium/calcium exchanger.* Nat Struct Mol Biol, 2016. **23**(6): p. 590-599.
14. Jiang, T., et al., *Computational Dissection of Membrane Transport at a Microscopic Level.* Trends Biochem Sci, 2020. **45**(3): p. 202-216.
15. Latorraca, N.R., et al., *Mechanism of Substrate Translocation in an Alternating Access Transporter.* Cell, 2017. **169**(1): p. 96-107 e12.
16. Zhao, C. and S.Y. Noskov, *The molecular mechanism of ion-dependent gating in secondary transporters.* PLoS Comput Biol, 2013. **9**(10): p. e1003296.
17. Moradi, M., G. Enkavi, and E. Tajkhorshid, *Atomic-level characterization of transport cycle thermodynamics in the glycerol-3-phosphate:phosphate antiporter.* Nat Commun, 2015. **6**: p. 8393.
18. Okazaki, K.I., et al., *Mechanism of the electroneutral sodium/proton antiporter PaNhaP from transition-path shooting.* Nat Commun, 2019. **10**(1): p. 1742.
19. Selvam, B., S. Mittal, and D. Shukla, *Free Energy Landscape of the Complete Transport Cycle in a Key Bacterial Transporter.* ACS Cent Sci, 2018. **4**(9): p. 1146-1154.
20. Blaustein, M.P. and W.J. Lederer, *Sodium/calcium exchange: its physiological implications.* Physiol Rev, 1999. **79**(3): p. 763-854.

21. DiPolo, R. and L. Beauge, *Sodium/calcium exchanger: influence of metabolic regulation on ion carrier interactions.* Physiol Rev, 2006. **86**(1): p. 155-203.
22. Clapham, D.E., *Calcium signaling.* Cell, 2007. **131**(6): p. 1047-58.
23. Berridge, M.J., M.D. Bootman, and H.L. Roderick, *Calcium signalling: dynamics, homeostasis and remodelling.* Nat Rev Mol Cell Biol, 2003. **4**(7): p. 517-29.
24. Ottolia, M., et al., *The Cardiac Na(+) -Ca(2+) Exchanger: From Structure to Function.* Compr Physiol, 2021. **12**(1): p. 2681-2717.
25. Khananshvili, D., *The SLC8 gene family of sodium-calcium exchangers (NCX) - structure, function, and regulation in health and disease.* Mol Aspects Med, 2013. **34**(2-3): p. 220-35.
26. Hilgemann, D.W., D.A. Nicoll, and K.D. Philipson, *Charge movement during Na+ translocation by native and cloned cardiac Na+/Ca2+ exchanger.* Nature, 1991. **352**(6337): p. 715-8.
27. Hilgemann, D.W., *Unitary cardiac Na+, Ca2+ exchange current magnitudes determined from channel-like noise and charge movements of ion transport.* Biophys J, 1996. **71**(2): p. 759-68.
28. Blaustein, M.P. and J.M. Russell, *Sodium-calcium exchange and calcium-calcium exchange in internally dialyzed squid giant axons.* J Membr Biol, 1975. **22**(3-4): p. 285-312.
29. Reeves, J.P. and C.C. Hale, *The stoichiometry of the cardiac sodium-calcium exchange system.* J Biol Chem, 1984. **259**(12): p. 7733-9.
30. Kimura, J., A. Noma, and H. Irisawa, *Na-Ca exchange current in mammalian heart cells.* Nature, 1986. **319**(6054): p. 596-7.
31. Rasgado-Flores, H. and M.P. Blaustein, *Na/Ca exchange in barnacle muscle cells has a stoichiometry of 3 Na+/1 Ca2+.* Am J Physiol, 1987. **252**(5 Pt 1): p. C499-504.
32. Kang, T.M. and D.W. Hilgemann, *Multiple transport modes of the cardiac Na+/Ca2+ exchanger.* Nature, 2004. **427**(6974): p. 544-8.
33. Shlosman, I., et al., *The prokaryotic Na(+)/Ca(2+) exchanger NCX_Mj transports Na(+) and Ca(2+) in a 3:1 stoichiometry.* J Gen Physiol, 2018. **150**(1): p. 51-65.
34. Crespo, L.M., C.J. Grantham, and M.B. Cannell, *Kinetics, stoichiometry and role of the Na-Ca exchange mechanism in isolated cardiac myocytes.* Nature, 1990. **345**(6276): p. 618-21.
35. Liao, J., et al., *Structural insight into the ion-exchange mechanism of the sodium/calcium exchanger.* Science, 2012. **335**(6069): p. 686-90.
36. Marinelli, F., et al., *Sodium recognition by the Na+/Ca2+ exchanger in the outward-facing conformation.* Proc Natl Acad Sci U S A, 2014. **111**(50): p. E5354-62.
37. John, S.A., et al., *The cardiac Na+-Ca2+ exchanger has two cytoplasmic ion permeation pathways.* Proc Natl Acad Sci U S A, 2013. **110**(18): p. 7500-5.
38. Waight, A.B., et al., *Structural basis for alternating access of a eukaryotic calcium/proton exchanger.* Nature, 2013. **499**(7456): p. 107-10.
39. Wu, M., et al., *Crystal structure of Ca2+/H+ antiporter protein YfkE reveals the mechanisms of Ca2+ efflux and its pH regulation.* Proc Natl Acad Sci U S A, 2013. **110**(28): p. 11367-72.

40. Nishizawa, T., et al., *Structural basis for the counter-transport mechanism of a H+/Ca2+ exchanger.* Science, 2013. **341**(6142): p. 168-72.
41. Marinelli, F. and J.D. Faraldo-Gomez, *Force-Correction Analysis Method for Derivation of Multidimensional Free-Energy Landscapes from Adaptively Biased Replica Simulations.* J Chem Theory Comput, 2021. **17**(11): p. 6775-6788.
42. Giladi, M., et al., *Dynamic distinctions in the Na(+)/Ca(2+) exchanger adopting the inward- and outward-facing conformational states.* J Biol Chem, 2017. **292**(29): p. 12311-12323.
43. Iwaki, M., et al., *Structure-affinity insights into the Na+ and Ca2+ interactions with multiple sites of a sodium-calcium exchanger.* The FEBS Journal. **n/a**(n/a).
44. Piana, S. and A. Laio, *A bias-exchange approach to protein folding.* J Phys Chem B, 2007. **111**(17): p. 4553-9.
45. Shindyalov, I.N. and P.E. Bourne, *Protein structure alignment by incremental combinatorial extension (CE) of the optimal path.* Protein Eng, 1998. **11**(9): p. 739-47.
46. *Schrödinger L.L.C. The PyMOL Molecular Graphics System, Version 2.3.4.* Schrödinger, 2015.
47. Almagor, L., et al., *Functional asymmetry of bidirectional Ca2+-movements in an archaeal sodium-calcium exchanger (NCX_Mj).* Cell Calcium, 2014. **56**(4): p. 276-84.
48. van Dijk, L., et al., *Key residues controlling bidirectional ion movements in Na(+)/Ca(2+) exchanger.* Cell Calcium, 2018. **76**: p. 10-22.
49. Emery, L., et al., *Protein Phylogenetic Analysis of Ca(2+)/cation Antiporters and Insights into their Evolution in Plants.* Front Plant Sci, 2012. **3**: p. 1.
50. Oganesyan, I., C. Lento, and D.J. Wilson, *Contemporary hydrogen deuterium exchange mass spectrometry.* Methods, 2018. **144**: p. 27-42.
51. Giladi, M., et al., *Asymmetric Preorganization of Inverted Pair Residues in the Sodium-Calcium Exchanger.* Sci Rep, 2016. **6**: p. 20753.
52. Bradshaw, R.T., et al., *Interpretation of HDX Data by Maximum-Entropy Reweighting of Simulated Structural Ensembles.* Biophys J, 2020. **118**(7): p. 1649-1664.
53. Best, R.B. and M. Vendruscolo, *Structural interpretation of hydrogen exchange protection factors in proteins: characterization of the native state fluctuations of CI2.* Structure, 2006. **14**(1): p. 97-106.
54. Zhang, Z. and D.L. Smith, *Determination of amide hydrogen exchange by mass spectrometry: a new tool for protein structure elucidation.* Protein Sci, 1993. **2**(4): p. 522-31.
55. Masson, G.R., et al., *Recommendations for performing, interpreting and reporting hydrogen deuterium exchange mass spectrometry (HDX-MS) experiments.* Nat Methods, 2019. **16**(7): p. 595-602.
56. Zhou, W., et al., *Large-scale state-dependent membrane remodeling by a transporter protein.* Elife, 2019. **8**.
57. Ren, X. and K.D. Philipson, *The topology of the cardiac Na(+)/Ca(2)(+) exchanger, NCX1.* J Mol Cell Cardiol, 2013. **57**: p. 68-71.
58. Forrest, L.R., C.L. Tang, and B. Honig, *On the accuracy of homology modeling and sequence alignment methods applied to membrane proteins.* Biophys J, 2006. **91**(2): p. 508-17.

59. Miguel, V., et al., *Molecular view of the interaction of S-methyl methanethiosulfonate with DPPC bilayer.* Biochim Biophys Acta, 2016. **1858**(1): p. 38-46.
60. Trosper, T.L. and K.D. Philipson, *Effects of divalent and trivalent cations on Na+-Ca2+ exchange in cardiac sarcolemmal vesicles.* Biochim Biophys Acta, 1983. **731**(1): p. 63-8.
61. Barthmes, M., et al., *Electrophysiological characterization of the archaeal transporter NCX_Mj using solid supported membrane technology.* J Gen Physiol, 2016. **147**(6): p. 485-96.
62. Weyand, S., et al., *Structure and molecular mechanism of a nucleobase-cation-symport-1 family transporter.* Science, 2008. **322**(5902): p. 709-13.
63. Faham, S., et al., *The crystal structure of a sodium galactose transporter reveals mechanistic insights into Na+/sugar symport.* Science, 2008. **321**(5890): p. 810-4.
64. Watanabe, A., et al., *The mechanism of sodium and substrate release from the binding pocket of vSGLT.* Nature, 2010. **468**(7326): p. 988-91.
65. Yamashita, A., et al., *Crystal structure of a bacterial homologue of Na+/Cl--dependent neurotransmitter transporters.* Nature, 2005. **437**(7056): p. 215-23.
66. Krishnamurthy, H. and E. Gouaux, *X-ray structures of LeuT in substrate-free outward-open and apo inward-open states.* Nature, 2012. **481**(7382): p. 469-74.
67. Malinauskaite, L., et al., *A conserved leucine occupies the empty substrate site of LeuT in the Na(+)-free return state.* Nat Commun, 2016. **7**: p. 11673.
68. Gotfryd, K., et al., *X-ray structure of LeuT in an inward-facing occluded conformation reveals mechanism of substrate release.* Nat Commun, 2020. **11**(1): p. 1005.
69. Kumar, H., et al., *Structure of sugar-bound LacY.* Proc Natl Acad Sci U S A, 2014. **111**(5): p. 1784-8.
70. Jiang, X., et al., *Crystal structure of a LacY-nanobody complex in a periplasmic-open conformation.* Proc Natl Acad Sci U S A, 2016. **113**(44): p. 12420-12425.
71. Verdon, G., et al., *Coupled ion binding and structural transitions along the transport cycle of glutamate transporters.* Elife, 2014. **3**: p. e02283.
72. Cai, X. and J. Lytton, *The cation/Ca(2+) exchanger superfamily: phylogenetic analysis and structural implications.* Mol Biol Evol, 2004. **21**(9): p. 1692-703.
73. Niggli, E. and W.J. Lederer, *Molecular operations of the sodium-calcium exchanger revealed by conformation currents.* Nature, 1991. **349**(6310): p. 621-4.
74. Baazov, D., X. Wang, and D. Khananshvili, *Time-resolved monitoring of electrogenic Na+-Ca2+ exchange in the isolated cardiac sarcolemma vesicles by using a rapid-response fluorescent probe.* Biochemistry, 1999. **38**(5): p. 1435-45.
75. Refaeli, B., R. Hiller, and D. Khananshvili, *Characteristic attributes limiting the transport rates in NCX orthologs.* Biochim Biophys Acta Biomembr, 2022. **1864**(1): p. 183792.
76. Vergara-Jaque, A., et al., *Repeat-swap homology modeling of secondary active transporters: updated protocol and prediction of elevator-type mechanisms.* Front Pharmacol, 2015. **6**: p. 183.
77. Sali, A. and J.P. Overington, *Derivation of rules for comparative protein modeling from a database of protein structure alignments.* Protein Sci, 1994. **3**(9): p. 1582-96.
78. Krivov, G.G., M.V. Shapovalov, and R.L. Dunbrack, Jr., *Improved prediction of protein side-chain conformations with SCWRL4.* Proteins, 2009. **77**(4): p. 778-95.

79. Staritzbichler, R., et al., *GRIFFIN: A versatile methodology for optimization of protein-lipid interfaces for membrane protein simulations.* J Chem Theory Comput, 2011. **7**(4): p. 1167-1176.
80. Phillips, J.C., et al., *Scalable molecular dynamics on CPU and GPU architectures with NAMD.* J Chem Phys, 2020. **153**(4): p. 044130.
81. MacKerell, A.D., et al., *All-atom empirical potential for molecular modeling and dynamics studies of proteins.* J Phys Chem B, 1998. **102**(18): p. 3586-616.
82. Mackerell, A.D., Jr., M. Feig, and C.L. Brooks, 3rd, *Extending the treatment of backbone energetics in protein force fields: limitations of gas-phase quantum mechanics in reproducing protein conformational distributions in molecular dynamics simulations.* J Comput Chem, 2004. **25**(11): p. 1400-15.
83. Hess, B., et al., *GROMACS 4: Algorithms for Highly Efficient, Load-Balanced, and Scalable Molecular Simulation.* J Chem Theory Comput, 2008. **4**(3): p. 435-47.
84. Bonomi, M., et al., *PLUMED: A portable plugin for free-energy calculations with molecular dynamics.* Computer Physics Communications, 2009. **180**(10): p. 1961-1972.
85. Bonomi, M., et al., *Promoting transparency and reproducibility in enhanced molecular simulations.* Nature Methods, 2019. **16**(8): p. 670-673.
86. Huang, J., et al., *CHARMM36m: an improved force field for folded and intrinsically disordered proteins.* Nat Methods, 2017. **14**(1): p. 71-73.
87. Klauda, J.B., et al., *Update of the CHARMM all-atom additive force field for lipids: validation on six lipid types.* J Phys Chem B, 2010. **114**(23): p. 7830-43.
88. Laio, A. and M. Parrinello, *Escaping free-energy minima.* Proc Natl Acad Sci U S A, 2002. **99**(20): p. 12562-6.
89. Bussi, G. and A. Laio, *Using metadynamics to explore complex free-energy landscapes.* Nature Reviews Physics, 2020. **2**(4): p. 200-212.
90. Branduardi, D., F.L. Gervasio, and M. Parrinello, *From A to B in free energy space.* J Chem Phys, 2007. **126**(5): p. 054103.
91. Emsley, P. and K. Cowtan, *Coot: model-building tools for molecular graphics.* Acta Crystallogr D Biol Crystallogr, 2004. **60**(Pt 12 Pt 1): p. 2126-32.
92. Adams, P.D., et al., *PHENIX: a comprehensive Python-based system for macromolecular structure solution.* Acta Crystallogr D Biol Crystallogr, 2010. **66**(Pt 2): p. 213-21.
93. Abraham, M., et al., *GROMACS: High performance molecular simulations through multi-level parallelism from laptops to supercomputers.* SoftwareX, 2015. **1–2**: p. 19-25.
94. Barducci, A., G. Bussi, and M. Parrinello, *Well-tempered metadynamics: A smoothly converging and tunable free-energy method.* Physical Review Letters, 2008. **100**(2).